Received: 29 November 2022 | Revised: 22 August 2023 | Accepted: 28 August 2023

DOI: 10.1002/esp.5701

RESEARCH ARTICLE

ESPL WILEY

Inland thinning of Byrd Glacier, Antarctica, during Ross Ice Shelf formation

Jamey Stutz[1] | Shaun Eaves[1,2] | Kevin Norton[1,2] | Klaus M. Wilcken[3] | Claudia Moore[1,2] | Rob McKay[1] | Dan Lowry[1,4] | Kathy Licht[5] | Katelyn Johnson[4]

[1]Antarctic Research Centre, Wellington, New Zealand

[2]School of Geography, Earth and Environmental Sciences, Te-Herenga Waka Victoria University of Wellington, Wellington, New Zealand

[3]ANSTO, Lucas Heights, NSW, Australia

[4]GNS Science, Lower Hutt, New Zealand

[5]Indiana University-Purdue University Indianapolis, Indianapolis, Indiana, USA

Correspondence
Jamey Stutz, Antarctic Research Centre, Wellington, New Zealand.
Email: jamey.stutz@vuw.ac.nz

Funding information
Antarctic Research Centre; Australian Institute of Nuclear Science and Engineering; Australian Nuclear Science and Technology Organisation, Centre for Accelerator Science, Grant/Award Number: AP12721; Ministry for Business Innovation and Employment

Abstract

Geomorphological records of past ice sheet change offer the opportunity to examine their centennial-scale response to changing boundary conditions, which are not adequately captured in the satellite record. Here, we present the first reconstruction of ice surface lowering at Byrd Glacier, the largest outlet glacier of the Transantarctic Mountains. Using surface exposure ages from glacial erratic cobbles collected in two vertical transects along the Lonewolf Nunataks, we find the initial emergence of this set of nunataks occurred at ~15 ka, with a rapid pulse of thinning at ~8 ka. We compare our glacier thinning profiles with modelled ice sheet thickness and grounding line histories from two model ensembles to identify key processes responsible for ice sheet change. All model runs from the two ensembles predict grounding line retreat and inland thinning to occur in one rapid step from Last Glacial Maximum to present, in line with marine geology records, our exposure age data and derived glacier thinning rates. Experiments best matching the glacial thickness constraints, reconstructed from the surface exposure data, have faster basal sliding (i.e., promote greater sliding rates resulting in thinner ice). However, experiments best matching the timing and rapid rate of ice thinning derived from the same surface exposure data have higher basal friction. This apparent change in the modelled basal sliding regime, from when the ice surface is at maximum thickness, to the rapid thinning at ~8 ka, occurs as the grounding line retreats towards the Byrd Glacier and Ross Ice Shelf forms during the Holocene. This past context has implications for the stability of the modern grounding line of Byrd Glacier, which is characterised by high basal melt rates at the terminus—a process that has the potential to propagate glacier thinning far inland, impacting the overall (in)stability of the Byrd Glacier and Ross Ice Shelf.

KEYWORDS
Antarctic ice sheet reconstruction, cosmogenic nuclides, data-model comparison, glacial geomorphology, surface exposure dating

1 | INTRODUCTION

By 2100, large sectors of the Antarctic Ice Sheet (AIS) may be affected by the abrupt onset of Marine Ice Sheet Instability (DeConto & Pollard, 2016; Fox-Kemper et al., 2021; Meredith et al., 2019). This process in which grounding lines retreat into deeper inland basins, and leading to dynamic thinning, has the potential to contribute up to an additional metre of sea level rise within the next century (Fox-Kemper et al., 2021; Schoof, 2007). Currently, relatively warm ocean water is thermally eroding ice shelves, driving widespread grounding line retreat and inland dynamic thinning (Fürst et al., 2016; Joughin et al., 2014; Pritchard et al., 2009, 2012; Smith et al., 2020). While the ongoing thinning of the AIS is dominated by mass loss along the Antarctic Peninsula and Amundsen Sea Sector (IMBIE, 2018), other

sectors, including the Ross Embayment, show evidence of localised extreme basal melt (Das et al., 2020; Stevens et al., 2020; Stewart et al., 2019), which could trigger inland thinning hundreds of kilometres away (Reese et al., 2018). Understanding the underlying processes responsible for future mass loss remains an important objective that is often addressed by comparing evidence for Holocene ice mass loss against ice sheet models.

In the Ross Embayment, the exact timing and pattern of grounding line retreat is debated due to a lack of reliable geological age constraints (Bart et al., 2018; Conway et al., 1999; Lee et al., 2017; R. McKay et al., 2016; Spector et al., 2017) and disagreement amongst models (Kingslake et al., 2018; Lowry et al., 2019). One scenario suggests that past ice shelf collapse may have caused the grounding line to retreat much farther inland than today and then readvanced to its current location (Kingslake et al., 2018; Venturelli et al., 2020). However, relative to the Weddell and Amundsen Sea Sectors, geological evidence for grounding line readvancement in the Ross Sea Sector is weak and inconsistent in the central Ross Sea embayment (Johnson et al., 2022). An alternate scenario is that grounding line retreat and stabilisation may have occurred in one step primarily in response to sea level rise, enhanced ocean heat and topographic controls from Last Glacial Maximum (LGM), ~20 000 years ago to present (Lowry et al., 2019). The vastly different retreat scenarios indicate that current ice sheet models do not fully capture all underlying ice mass loss processes. Importantly, past modelled retreat scenarios are driven by the same models that forecast Antarctica's future ice mass loss and contribution to sea level rise, therefore, these disparities have implications for the forecasts themselves (Chambers et al., 2022; DeConto & Pollard, 2016; Golledge et al., 2015; Seroussi et al., 2020). Current observations of enhanced melt beneath modern Antarctic ice shelves, possibly initiating Marine Ice Sheet Instability, emphasise the urgent need to understand the pattern and drivers for past AIS mass loss so that ice sheet models, and thereby future projections, are improved.

Cosmogenic nuclide inventories extracted from glacial debris have revolutionised our ability to reconstruct the past AIS, providing critical thickness constraints on past ice margins (Balco, 2011; Small et al., 2019). Entrained glacial debris is ultimately deposited by a thinning glacier, at which point cosmogenic nuclide production begins and offers a way to determine the samples surface exposure age, or time since deposition. Exposure ages from glacial debris, collected along a vertical transect, typically show a lower exposure age with elevation and this trend is interpreted to reflect past ice thickness changes (Small et al., 2019; Stone et al., 2003). By combining terrestrial and marine records of past ice fluctuations, a clear early-mid Holocene ice thinning and grounding line retreat signal has emerged (Bentley et al., 2014). Despite two decades of reconstructions of the past AIS using cosmogenic nuclides, vast regions, particularly those of the continental interior, remain unconstrained.

The Byrd Glacier basin (Figure 1) is one of the largest glacier catchments on Earth (1.07×10^6 km^2) and responsible for ~18% of the total ice flux to the Ross Ice Shelf (Stearns et al., 2008). Consequently, it represents a significant element of the past AIS with an unconstrained onshore thinning history. Submarine mapping and sediment provenance studies show that, during the LGM, the Byrd Glacier advanced along with other outlet glaciers into the outer Ross Sea (Bentley et al., 2014; Licht & Palmer, 2013). At the LGM, the Byrd Glacier filled the Central Basin, JOIDES and Pennell troughs and Glomar Challenger Basin (Halberstadt et al., 2016; Licht & Palmer, 2013) (Figure 1a). Subsequent grounding line retreat in the outer Pennell Trough was initiated sometime just prior to 15 ka (Prothro et al., 2020) with two

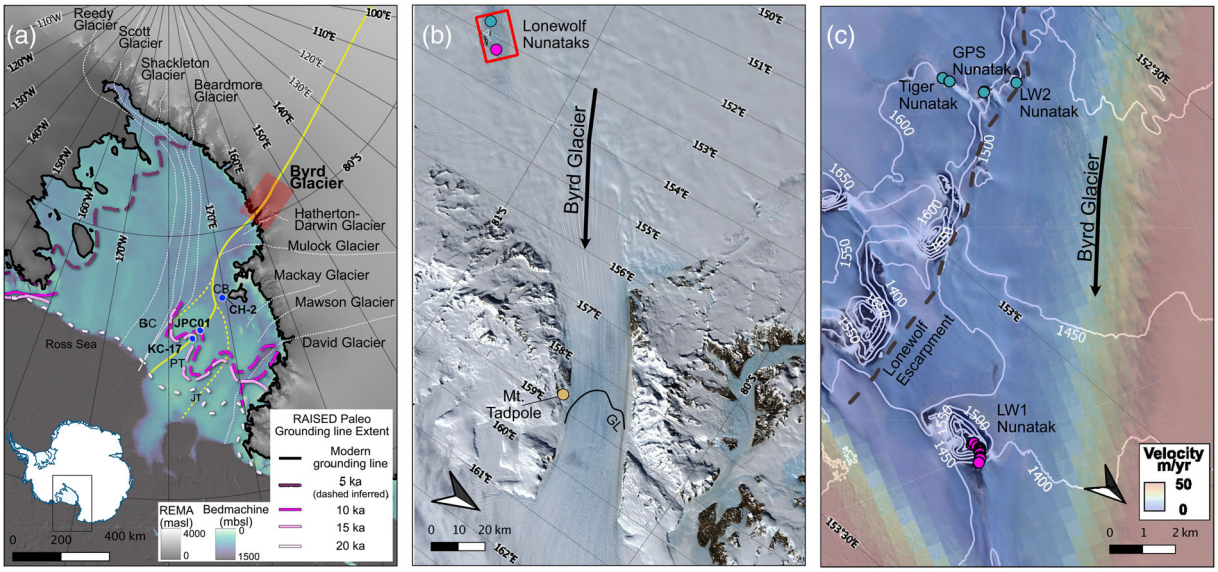

FIGURE 1 (a) Overview map of topography (Howat et al., 2019) and bathymetry (Morlighem et al., 2020) of the Ross Embayment and Transantarctic Mountains (TAM) including feature names mentioned in the text: Glomar Challenger Basin (GCB), JOIDES Trough (JT), Pennell Trough (PT), Central Basin (CB). Shaded red box indicates extent of panel b. Magenta lines show paleo grounding line extent (J. B. Anderson et al., 2014; Bentley et al., 2014) and black line shows modern grounding line location. Thin white lines and yellow line indicate flowline paths associated with Figure 9. Note location of cores KC17, JPC01 (Prothro et al., 2020) and CH-2 (R. McKay et al., 2016). (b) Satellite image (Bindschadler et al., 2008) of Byrd Glacier as it flows through the TAM. Red box indicates extent of panel c. Note the location of field sites of this study and the location of the modern day grounding line (GL). (c) Satellite image (Bindschadler et al., 2008) and topographic contours (Howat et al., 2019) of the Lonewolf Nunataks. Black dashed line indicates location of Lonewolf Escarpment. Samples collected in the field are indicated with filled circles.

pulses of thinning (14–10 and 10–7 ka) (Anderson et al., 2017) and open marine conditions east of Ross Island established by 8.6 ka (McKay et al., 2016). During deglaciation, ice sheet modelling suggests that debuttressing of thick grounded ice caused the Byrd Glacier to speed up and ice shelf area is likely to have rapidly expanded over the deeper topography south of Ross Island, thus playing a significant role in early formation of the Ross Ice Shelf (Lowry et al., 2019) (Figure 2). While earlier studies provide some constraints on the outer Ross Sea history of past marine ice sheets sourced from Byrd Glacier catchment, the inland history along the Byrd Glacier represents a significant gap in constraining this sector of the AIS.

In this study, we assess the response of upper Byrd Glacier to grounding line retreat in the Ross Sea, the pacing of surface lowering compared with other Transantarctic Mountain (TAM) outlet glaciers and how its thinning history compares with those predicted by ice sheet models. We achieve this by collecting glacial erratics in vertical transects from the modern ice surface to the highest local peak and extract inventories of cosmogenic nuclides to calculate surface exposure ages. Next, we use the calculated ^{10}Be surface exposure age of a glacial erratic to constrain the ice surface elevation over time (Small et al., 2019; Stone et al., 2003). We compile all exposure age-elevation pairs to track the thinning history for each sampling site. These paleo-thinning rates are then compared against rates simulated in two separate ensembles of transient deglacial ice sheet model experiments for the Ross Sea region. Finally, we examine the broader pattern of grounding line retreat in these model ensembles to provide a physical basis to help explain the emerging regional pattern of Transantarctic outlet glacier response to deglaciation.

2 | METHODOLOGY AND METHODS

2.1 | Cosmogenic nuclide sample collection and processing

Field work was conducted during the 2019–2020 austral summer season and included two visits to the Lonewolf Nunataks, an archipelago of nunataks approximately 150 km inland from the modern grounding line of Byrd Glacier (Figure 1b). There are six individual nunataks in the group with a prominent topographic escarpment extending along the northern margin of the nunatak group (Figure 1c). Above the escarpment, slow ice surface velocities and ablation features such as blue ice and wind scoops dominate while below the escarpment, fast ice surface velocities, flow stripes and crevassing dominate (Bindschadler et al., 2008; Rignot et al., 2011). Using a Trimble GeoXH GPS, we collected 28 quartz rich glacial erratic cobbles perched on

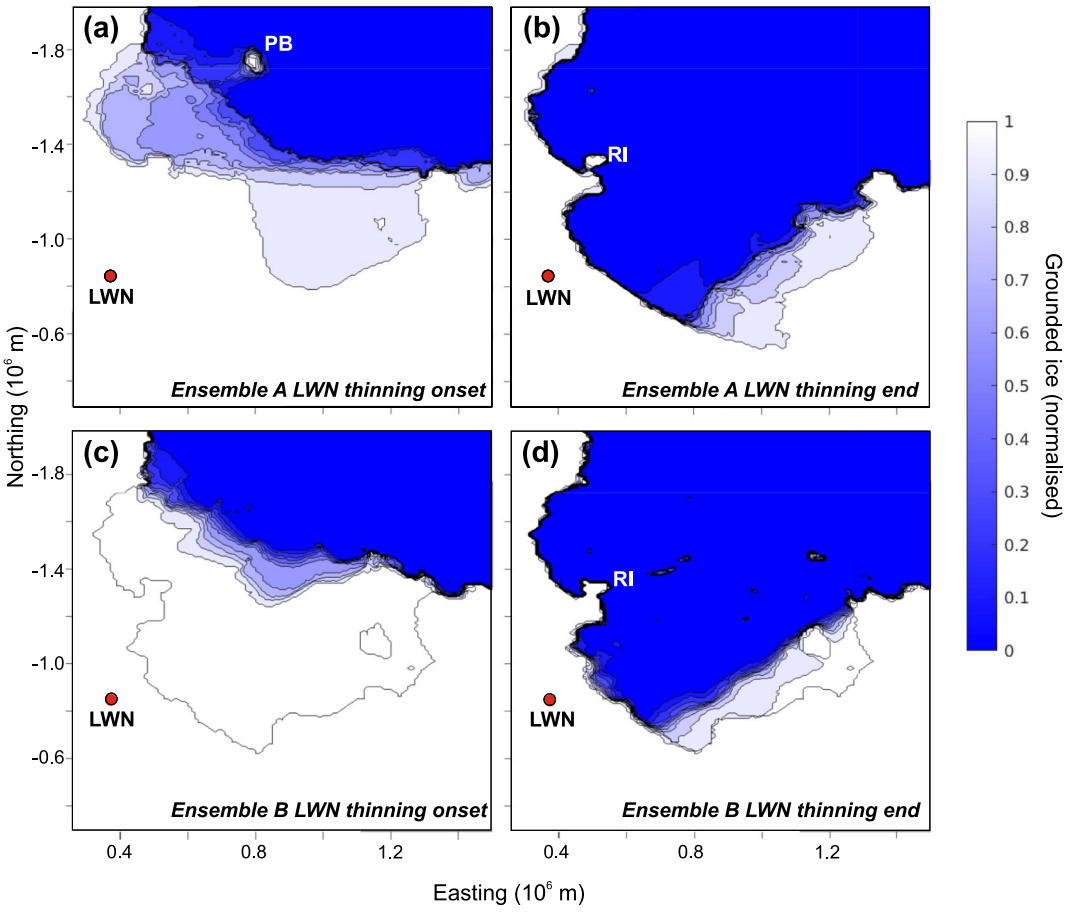

FIGURE 2 Modelled evolution of grounded ice in the Ross Sea during ice sheet thinning at Lonewolf Nunataks (LWN) as simulated by the model ensemble A (panels a and b; Lowry et al., 2019, 2020) and model ensemble B (panels c and d; Hillebrand et al., 2021). Panels a and c represent grounded ice distribution at the onset of modelled thinning at Lonewolf Nunataks (LWN), while panels b and d show the distribution of grounded ice immediately after modelled thinning ceases at LWN. Grounded ice is normalised to represent the fraction of model ensemble members (i.e., 1 = all members show grounded ice, 0 = no members show grounded ice). Other key locations indicated: RI = Ross Island, PB = Pennell Bank.

bedrock in two vertical transects from the modern ice surface to the highest local peaks, spread across three sample sites. Cobbles commonly had bulleted shape with facets and rarely glacial striae. The first vertical transect spans elevations between 1392 to 1634 metres above sea level (m.a.s.l) and consists of samples from the Lonewolf 1 (LW) Nunatak. LW1 Nunatak is situated below the prominent topographic escarpment in a zone of enhanced ice flow velocities (Rignot et al., 2011). The second vertical transect is located further upstream, spans elevations of 1671 to 1420 m.a.s.l. and consists of samples from three nunataks (Tiger, GPS and Lonewolf 2 [LW2]) that are all located above the escarpment (Figures 3 and 4). We incorporate and exposure date previously collected glacial erratic cobbles from LW2 moraine deposit (Palmer et al., 2012) and Mt. Tadpole (Figures 3c and S3) within the Byrd Fiord.

Samples were crushed, sieved and magnetically separated on the Frantz isodynamic electromagnet. Quartz separates were chemically leached in 10% HCl for 24–48 h followed by two rounds of 1% HF for 4–5 days each round. Quartz purity was tracked visually via microscope throughout sample processing. Approximately 250 µg of ^{9}Be spike was added and sample digestion, ion exchange chemistry and sample conversion followed established methods (Norton et al., 2008). Following calcination by open flame, the BeO was mixed with Nb powder and pressed into copper cathodes. Measurements of ^{10}Be/^{9}Be was completed by Accelerator Mass Spectrometry on the 6 MV Sirius Accelerator at the Australia Nuclear Science Technology Organisation (Wilcken et al., 2019). Measured ^{10}Be concentrations were normalised to the KN-5-3 standard with a reference value for ^{10}Be/^{9}Be ratio of 6.320e−12 (t1/2 = 1.36 Myr) (Nishiizumi et al., 2007). The measured ^{10}Be concentrations were blank corrected following standard procedures as in (Balco et al., 2008; Wilcken et al., 2022). Surface exposure ages were calculated, accounting for local topographic shielding and assuming zero erosion, with the online cosmogenic nuclide calculator (Version 3) (Balco et al., 2008) and the LSDn scaling scheme (Lifton et al., 2014) (Tables 1–4).

Using the 'estimate linear thinning rate' tool (Jones et al., 2019), we combine exposure ages from each transect to reconstruct paleothinning rates (Jones et al., 2019; Small et al., 2019). This approach performs least-squares regression analysis for a suite of exposure ages through a Monte Carlo simulation and assumes exposure ages marks the ice surface at each position and thinning was continuous over the transect (Jones et al., 2019). To determine elevation above modern ice surface (i.e., for thickness change and thinning rate calculations) along a transect, we subtract the nearest elevation of the glacier, within the zone of enhanced ice velocities, from the sample elevation.

2.2 | Methods (ice sheet modelling setup)

Using the output from two 3-dimensional thermomechanical ice sheet models, namely, the Parallel Ice Sheet Model (Bueler & Brown, 2009)

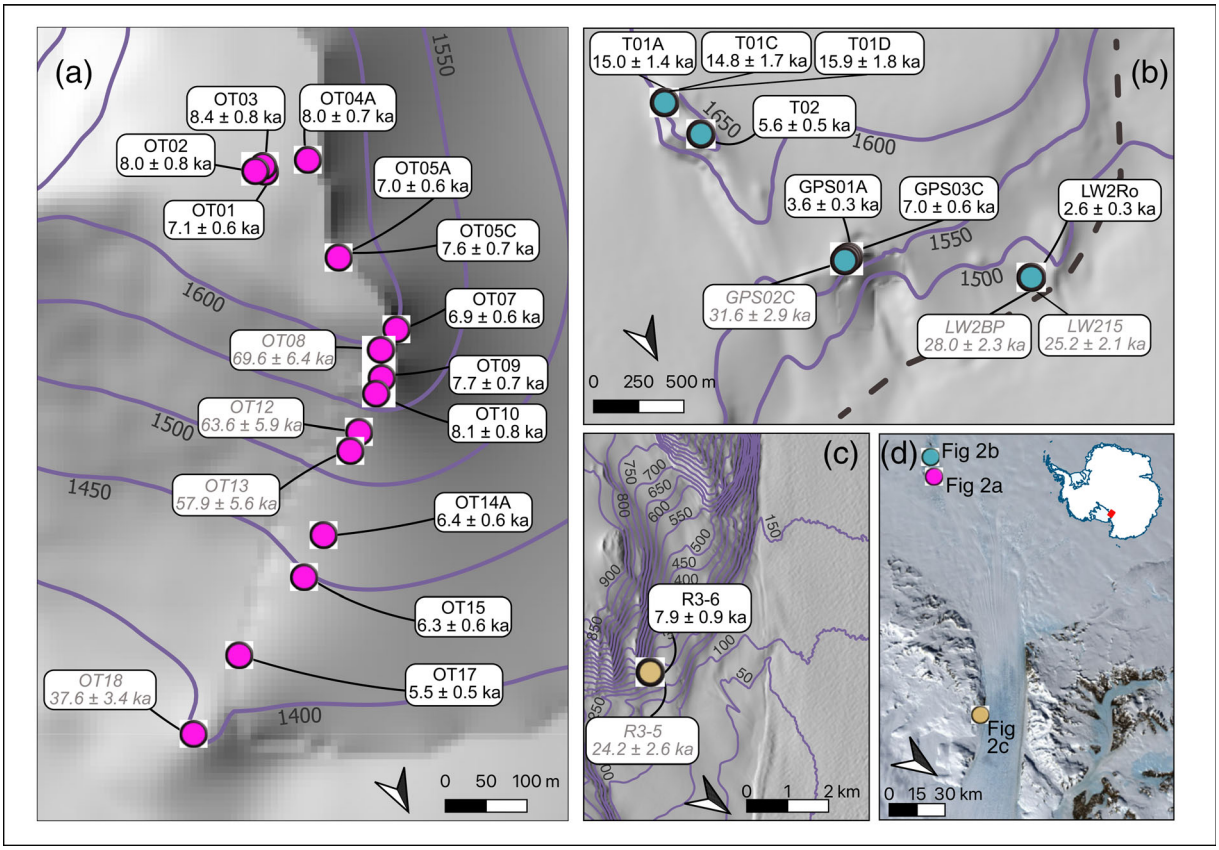

FIGURE 3 Hillshade map, elevation contours in metres above sea level (Howat et al., 2019) of (a) LW1 Nunatak, (b) Tiger-GPS Nunataks and (c) Mt. Tadpole. All samples are reported with sample name, exposure age and total uncertainty including analytical error and errors arising from production rate calibration and scaling to sites (Balco et al., 2008). Samples labelled with grey text indicate samples interpreted to contain inherited cosmogenic nuclide inventory due to previous exposure, (d) satellite image (Bindschadler et al., 2008) showing location of a, b, and c. Dashed grey line in B is location of Lonewolf Escarpment.

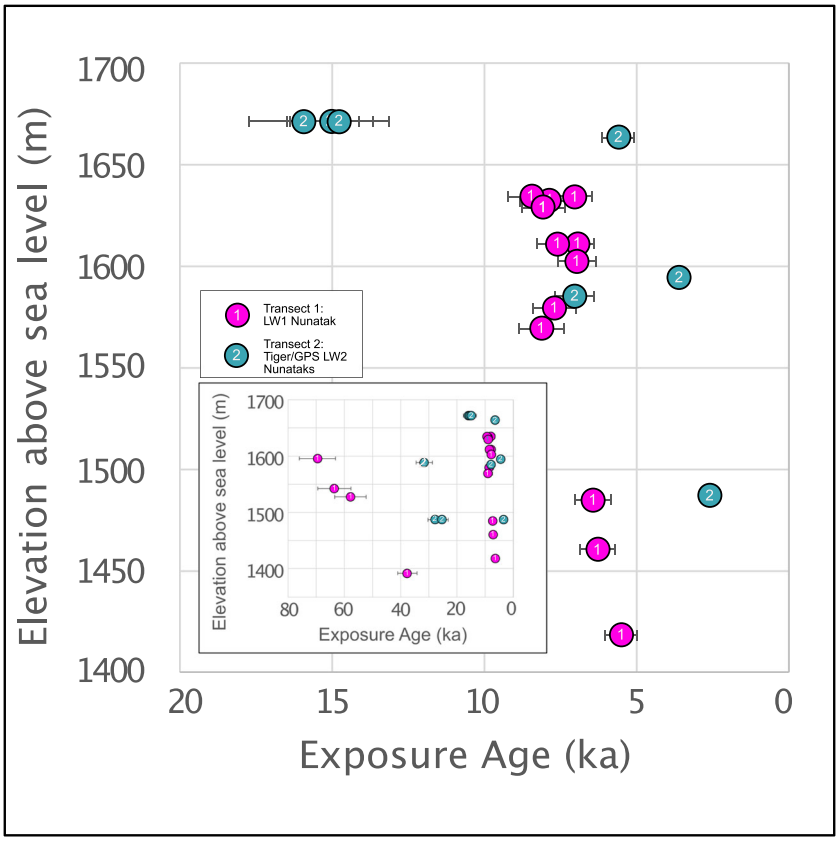

FIGURE 4 Elevation (metres above sea level) versus calculated exposure ages and total uncertainty (including analytical error and errors arising from production rate calibration and scaling to sites) for all LGM to present samples in this study. Inset shows all exposure age data for this study.

and Pennsylvania State University 3-D Ice Sheet Model (Pollard & Deconto, 2012), we extract the modelled ice sheet thinning and grounding line retreat histories from two ensembles of the last deglaciation for the Lonewolf Nunataks (Hillebrand et al., 2021; Lowry et al., 2019, 2020). These ensembles are chosen because they cover the necessary geographic domain to investigate the relationship between regional grounding line dynamics and ice thinning at Byrd Glacier. Both model ensembles use a hybrid combination of Shallow Ice Approximation (SIA) and/Shallow Shelf Approximation (SSA) equations for ice flow. They also consider uncertainty in other model parameters that impact the timing of deglacial ice sheet retreat. We refer to these respective model ensembles as model ensemble A and model ensemble B.

Model ensemble A (Lowry et al., 2019, 2020) is run at 10-km horizontal resolution for the Ross Sea catchment only. This ensemble includes simulations with different climate forcings to explore the effect of timing and magnitude of deglacial warming. These forcings are based on WAIS divide (Cuffey et al., 2016) and EPICA Dome C (Parrenin et al., 2007) ice core records, benthic d18O records (Elderfield et al., 2012; Lisiecki & Raymo, 2005) and climate model outputs (Liu et al., 2009; Menviel et al., 2011). The ocean forcing is applied uniformly to the ice shelf as a basal melt rate anomaly scaled from LGM to present (Lowry et al., 2019).

The ensemble also includes simulations with different model parameters values to explore the uncertainties of ice rheology, basal friction and Glacial Isostatic Adjustment (GIA) (Lowry et al., 2020):

- ESIA: enhancement factor of the stress balance in SIA; ice deforms more easily in shear with increasing values
- ESSA: enhancement factor of the stress balance in SSA; lower values result in slower/thicker ice streams and ice shelves
- q: exponent used in the pseudo-plastic sliding law; Ranges from 0 (plastic sliding) to 1 (linear sliding)
- Mantle viscosity: The ice sheet model includes a solid Earth model (Lingle & Clark, 1985). Mantle viscosity influences the rate of GIA
- Minimum till friction angle on the continental shelf (i.e., where current ice shelves are)—"marine" sediments are weaker than "continental" bedrock. This term impacts the yield stress.

Model ensemble B (Hillebrand et al., 2021) is run at 20- and 10-km resolution for the full continent. Ice shelf melt rates are calculated from ocean temperatures (Liu et al., 2009), with atmospheric forcing scaled from benthic d18O records. The ensemble includes runs with varied values for four model parameters and two different sea level curves (Lisiecki & Raymo, 2005; Lisiecki & Stern, 2016).

- Basal sliding coefficient of the seafloor (different than q above, but also impacts ice sheet sliding)
- Isostatic rebound rate (different than MV above, but also influences GIA)
- Melt rate sensitivity factor (to ocean temperature)
- Calving rate factor

3 | RESULTS

3.1 | Transect 1: LW1 Nunatak

Results from LW1 Nunatak provide exposure ages tracking the upper ice surface from ~8.4 to 5.5 ka and records a total thickness change of ~270 m (Figures 3a and 4). The uppermost samples, collected from a broad plateau-like area, show a range of exposure ages from 8.4 to

TABLE 1 AMS data and blank correction for ^{10}Be measurements in this study. First eight rows are procedural blanks used to calculate ^{10}Be concentrations in associated samples. Headers indicate sample name, quartz mass, carrier added, ^{10}Be/^{9}Be ratio measured, ^{10}Be concentrations and associated uncertainties.

Process blank #	Qtz mass (g)	Carrier added (g)	^{9}Be blank (g)	^{9}Be uncertainty (g)	10/9 blank ratio	10/9 blank ratio uncertainty	^{10}Be blank (at)	^{10}Be blank uncertainty (at)	% uncertainty
OT-B1	n.a.	0.308	3.09E−04	3.46E−06	2.2E−15	3.1E−16	46 480	6449	13.8
OT-B2	n.a.	0.310	3.11E−04	3.48E−06	1.0E−15	2.0E−16	20 982	4135	19.7
GPS-B	n.a.	0.358	3.59E−04	4.01E−06	2.7E−15	3.1E−16	64 522	7557	11.7
EHW-B	n.a.	0.359	3.61E−04	4.03E−06	5.8E−15	4.3E−16	139 053	10 544	7.5
EHW-B2	n.a.	0.359	3.60E−04	4.02E−06	3.4E−15	7.7E−16	81 363	18 500	22.7
OT-B2_2	n.a.	0.358	3.59E−04	4.01E−06	1.9E−15	2.2E−16	46 634	5280	11.3
TigerB	n.a.	0.311	3.12E−04	3.49E−06	4.8E−15	4.4E−16	100 674	9328	9.2
Sample #	**Qtz mass (g)**	**Carrier added (g)**	**^{9}Be (g)**	**^{9}Be uncertainty (g)**	**10/9 ratio**	**10/9 ratio uncertainty**	**^{10}Be conc. (at/g)**	**^{10}Be conc. uncertainty**	**% uncertainty**
Batch OT-B1									
OT-01	25.573	0.307	3.08E−04	3.44E−06	2.1E−13	4.8E−15	171 225	4302	2.2
OT-05A	25.881	0.307	3.08E−04	3.44E−06	2.1E−13	4.6E−15	165 276	4112	2.2
OT-07	25.859	0.308	3.09E−04	3.45E−06	2.1E−13	4.4E−15	163 295	3986	2.1
OT-14A	24.668	0.307	3.09E−04	3.45E−06	1.6E−13	4.0E−15	134 897	3693	2.5
OT-17	25.110	0.307	3.09E−04	3.45E−06	1.4E−13	3.5E−15	110 332	3146	2.6
Batch OT-B2									
OT-10	14.741	0.377	3.79E−04	4.23E−06	1.1E−13	2.7E−15	183 022	5043	2.5
OT-15	13.711	0.307	3.08E−04	3.44E−06	8.7E−14	2.2E−15	128 908	3580	2.5
Batch GPS-B									
OT-18	18.267	0.356	3.57E−04	3.99E−06	5.6E−13	1.3E−14	731 790	18 893	2.3
T-01	9.506	0.356	3.58E−04	3.99E−06	1.5E−13	3.5E−15	373 348	9804	2.3
T-02	12.972	0.357	3.58E−04	4.00E−06	7.7E−14	1.9E−15	136 328	3850	2.5
GPS-01A	22.550	0.357	3.58E−04	4.00E−06	8.2E−14	2.0E−15	84 493	2354	2.4
GPS-03C	17.520	0.358	3.59E−04	4.01E−06	1.2E−13	2.7E−15	161 954	4118	2.2
Batch_EHWB									
LW2-BP	18.992	0.357	3.59E−04	4.01E−06	4.3E−13	7.3E−15	538 704	11 070	1.7
LW2-Ro	18.077	0.357	3.59E−04	4.01E−06	4.5E−14	1.2E−15	51 396	1831	2.7
Batch_EHWB2									
R3-5	12.164	0.359	3.61E−04	4.03E−06	8.8E−14	2.2E−15	168 377	5101	2.5
R3-6	13.699	0.359	3.60E−04	4.03E−06	3.5E−14	1.1E−15	55 920	2470	3.2
LW2-15	13.738	0.359	3.61E−04	4.03E−06	2.8E−13	4.8E−15	486 624	10 074	1.7
Batch OTB2_2									
OT-02	8.220	0.358	3.60E−04	4.02E−06	6.7E−14	1.9E−15	189 873	5899	2.8
OT-03	13.540	0.358	3.59E−04	4.01E−06	1.2E−13	2.7E−15	200 630	5382	2.4
OT-04A	14.413	0.358	3.60E−04	4.02E−06	1.2E−13	2.6E−15	189 591	4824	2.2
OT-05c	13.787	0.358	3.59E−04	4.01E−06	1.0E−13	2.3E−15	176 631	4499	2.2
OT-08	13.583	0.359	3.60E−04	4.03E−06	8.8E−13	2.1E−14	1 559 170	41 051	2.4
OT-09	13.476	0.358	3.59E−04	4.01E−06	1.0E−13	2.4E−15	174 763	4700	2.4
OT-12	6.199	0.359	3.60E−04	4.02E−06	3.5E−13	8.4E−15	1 365 404	36 106	2.4
OT-13	7.621	0.358	3.60E−04	4.02E−06	3.9E−13	1.1E−14	1 224 459	35 933	2.7
GPS02C	9.170	0.359	3.61E−04	4.03E−06	2.7E−13	6.5E−15	711 721	18 850	2.4
Batch TigerB									
T01C	2.312	0.311	3.12E−04	3.49E−06	4.5E−14	1.5E−15	359 247	14 755	3.3
T01D	1.989	0.311	3.12E−04	3.48E−06	4.2E−14	1.4E−15	384 465	15 821	3.3

TABLE 2 Sample metadata (location, thickness, density, shielding, erosion) and ^{10}Be concentration, formatted for the online cosmogenic nuclide calculator (V3).

Sample	Long	Lat	Elev	Pres	Thickness	Density	Shielding	Erosion	Year	
OT01	−81.285307	153.225085	1634.714	Ant	1.91	2.3	0.9923	0	2019	;
OT02	−81.285372	153.225027	1632.385	Ant	3.50	2.7	0.9800	0	2019	;
OT03	−81.285362	153.225665	1634.338	Ant	3.50	2.3	0.9800	0	2019	;
OT04A	−81.28521	153.221907	1629.108	Ant	3.50	2.7	0.9800	0	2019	;
OT05A	−81.2841	153.223108	1611.366	Ant	2.44	2.3	0.9923	0	2019	;
OT05C	−81.2841	153.223108	1611.366	Ant	3.50	2.3	0.9800	0	2019	;
OT07	−81.283113	153.221711	1602.697	Ant	1.98	2.3	0.9923	0	2019	;
OT08	−81.282989	153.223401	1595.895	Ant	3.50	2.3	0.9800	0	2019	;
OT09	−81.28271	153.224258	1579.55	Ant	3.50	2.3	0.9800	0	2019	;
OT10	−81.282584	153.225129	1569.281	Ant	4.35	2.7	0.9923	0	2019	;
OT12	−81.282293	153.227478	1542.506	Ant	3.50	2.3	0.9800	0	2019	;
OT13	−81.28215	153.22865	1527.657	Ant	3.50	2.7	0.9800	0	2019	;
OT14A	−81.281456	153.233126	1484.729	Ant	3.78	2.3	0.9923	0	2019	;
OT15	−81.281141	153.235754	1460.355	Ant	3.63	2.7	0.9923	0	2019	;
OT17	−81.280698	153.242471	1418	Ant	2.22	2.3	0.9923	0	2019	;
OT18	81.2801504	153.247993	1392	Ant	2.15	2.7	0.9923	0	2019	;
GPS01A	−81.346045	152.729507	1594.664	Ant	2.75	2.3	0.9900	0	2019	;
GPS02C	−81.346038	152.730276	1588.701	Ant	3.50	2.3	0.9800	0	2019	;
GPS03C	−81.345982	152.731101	1585.117	Ant	2.50	2.3	0.9900	0	2019	;
T01A	−81.357061	152.760153	1671.72	Ant	1.50	2.3	0.9900	0	2019	;
T01C	−81.357061	152.760153	1671.72	Ant	3.50	2.3	0.9800	0	2019	;
T01D	−81.357061	152.760153	1671.72	Ant	3.50	2.7	0.9800	0	2019	;
T02	−81.355038	152.75666	1663.72	Ant	2.75	2.7	0.9900	0	2019	;
LW2BP	−81.341	152.679	1420	Ant	5.05	2.7	0.9800	0	2005	;
LW2Ro	−81.341	152.679	1420	Ant	3.52	2.7	0.9800	0	2005	;
LW215	−81.341	152.679	1420	Ant	4.86	2.7	0.9800	0	2005	;
R3-5	−80.501827	158.72932	306	Ant	5.70	2.7	0.9800	0	2010	;
R3-6	−80.501827	158.72932	306	Ant	5.40	2.7	0.9800	0	2010	;
OT01	Be-10	Quartz	1.712E+05	4.302E+03	07KNSTD	;				
OT02	Be-10	Quartz	1.899E+05	5.899E+03	07KNSTD	;				
OT03	Be-10	Quartz	2.006E+05	5.382E+03	07KNSTD	;				
OT04A	Be-10	Quartz	1.896E+05	4.824E+03	07KNSTD	;				
OT05A	Be-10	Quartz	1.653E+05	4.112E+03	07KNSTD	;				
OT05c	Be-10	Quartz	1.766E+05	4.499E+03	07KNSTD	;				
OT07	Be-10	Quartz	1.633E+05	3.986E+03	07KNSTD	;				
OT08	Be-10	Quartz	1.559E+06	4.105E+04	07KNSTD	;				
OT09	Be-10	Quartz	1.748E+05	4.700E+03	07KNSTD	;				
OT10	Be-10	Quartz	1.830E+05	5.043E+03	07KNSTD	;				
OT12	Be-10	Quartz	1.365E+06	3.611E+04	07KNSTD	;				
OT13	Be-10	Quartz	1.224E+06	3.593E+04	07KNSTD	;				
OT14A	Be-10	Quartz	1.349E+05	3.693E+03	07KNSTD	;				
OT15	Be-10	Quartz	1.289E+05	3.580E+03	07KNSTD	;				
OT17	Be-10	Quartz	1.103E+05	3.146E+03	07KNSTD	;				
OT18	Be-10	Quartz	7.318E+05	1.889E+04	07KNSTD	;				
GPS01A	Be-10	Quartz	8.449E+04	2.354E+03	07KNSTD	;				
GPS02C	Be-10	Quartz	7.117E+05	1.885E+04	07KNSTD	;				
GPS03C	Be-10	Quartz	1.620E+05	4.118E+03	07KNSTD	;				
T01A	Be-10	Quartz	3.733E+05	9.804E+03	07KNSTD	;				
T01C	Be-10	Quartz	3.592E+05	1.475E+04	07KNSTD	;				

(Continues)

TABLE 2 (Continued)

Sample	Long	Lat	Elev	Pres	Thickness	Density	Shielding	Erosion	Year
T01D	Be-10	Quartz	3.845E+05	1.582E+04	07KNSTD	;			
T02	Be-10	Quartz	1.363E+05	3.850E+03	07KNSTD	;			
LW2BP	Be-10	Quartz	5.387E+05	1.107E+04	07KNSTD	;			
LW2Ro	Be-10	Quartz	5.140E+04	1.831E+03	07KNSTD	;			
LW215	Be-10	Quartz	4.866E+05	1.007E+04	07KNSTD	;			
R3-5	Be-10	Quartz	1.684E+05	5.101E+03	07KNSTD	;			
R3-6	Be-10	Quartz	5.592E+04	2.470E+03	07KNSTD	;			

TABLE 3 Sample surface exposure age for three scaling schemes as part of the online cosmogenic nuclide calculator.

		St			Lm			LSDn		
Sample name	Nuclide	Age (year)	Interr (year)	Exterr (year)	Age (year)	Interr (year)	Exterr (year)	Age (year)	Interr (year)	Exterr (year)
OT01	Be-10 (qtz)	7762	195	645	7538	190	597	7086	178	455
OT02	Be-10 (qtz)	8872	276	755	8616	268	701	8040	250	537
OT03	Be-10 (qtz)	9319	251	779	9049	243	722	8441	227	548
OT04A	Be-10 (qtz)	8880	226	739	8624	220	684	8049	205	518
OT05A	Be-10 (qtz)	7658	191	635	7437	185	589	7002	175	449
OT05c	Be-10 (qtz)	8348	213	694	8107	207	643	7587	194	489
OT07	Be-10 (qtz)	7592	186	629	7372	180	583	6947	170	444
OT08	Be-10 (qtz)	75 849	2036	6437	73 623	1975	5961	69 566	1864	4574
OT09	Be-10 (qtz)	8470	228	708	8225	222	657	7704	208	500
OT10	Be-10 (qtz)	8931	247	749	8673	239	694	8117	224	530
OT12	Be-10 (qtz)	69 114	1860	5858	67 089	1805	5426	63 550	1708	4175
OT13	Be-10 (qtz)	62 873	1875	5383	61 033	1819	4991	57 851	1723	3868
OT14A	Be-10 (qtz)	6965	191	583	6764	185	541	6414	176	418
OT15	Be-10 (qtz)	6808	189	571	6612	184	530	6278	175	410
OT17	Be-10 (qtz)	5940	170	500	5768	165	464	5496	157	361
OT18	Be-10 (qtz)	40 665	1061	3414	39 482	1029	3163	37 629	981	2446
GPS01A	Be-10 (qtz)	3980	111	334	3865	108	310	3599	100	235
GPS02C	Be-10 (qtz)	34 463	921	2896	33 462	894	2684	31 606	844	2060
GPS03C	Be-10 (qtz)	7681	196	639	7459	190	592	7031	179	452
T01A	Be-10 (qtz)	16 476	435	1377	16 000	422	1277	15 017	396	973
T01C	Be-10 (qtz)	16 243	670	1452	15 773	650	1354	14 803	610	1068
T01D	Be-10 (qtz)	17 467	722	1563	16 962	701	1457	15 924	658	1150
T02	Be-10 (qtz)	6112	173	514	5935	168	476	5588	158	366
LW2BP	Be-10 (qtz)	30 277	629	2491	29 399	610	2304	27 970	580	1760
LW2Ro	Be-10 (qtz)	2833	101	246	2751	98	229	2558	91	176
LW215	Be-10 (qtz)	27 286	569	2244	26 495	552	2075	25 201	525	1586
R3-5	Be-10 (qtz)	25 555	779	2176	24 820	757	2020	24 204	738	1615
R3-6	Be-10 (qtz)	8429	373	765	8187	362	714	7918	351	585

7 ka, with a weighted mean age of 7.9 ± 0.5 ka (Figures 5a and Figure S1). Samples collected along a ridge leading to the modern ice surface show Holocene exposure ages from ~8 to 5.5 ka. Samples OT-08, -12, -14 and -18 show exposure ages older than the LGM and are interpreted to represent inheritance of cosmogenic nuclides from prior exposure. Samples OT-9 and -10, collected on a sharp change in slope, show older than expected but still Holocene exposure ages, potentially related to local factors such as down slope displacement or earlier exposure during deglaciation.

3.2 | Transect 2: Tiger-GPS-LW2 Nunataks

Surface exposure ages from three sites along the composite transect record ~15 kyr of ice thinning (Figures 3 and 4). The highest elevation samples (Tiger1A–C) found at 1671 m.a.s.l record thickness changes of ~190 m, have exposure ages between 14.8 and 15.9 ka ($n = 3$; weighted mean: 15.2 ± 0.5 ka) and are interpreted here to constrain the initial emergence of this nunatak (Figure 5b). Subsequent thinning is constrained with mid-Holocene ages from lower elevations. The

TABLE 4 Relevant sample metadata (latitude, longitude, elevation, relative elevation) and exposure age.

Sample name	Lat	Long	Elev	RelativeElev	Age (kyr)	Total error (kyr)	Site name	Lithology	Type	Geomorphical position
OT01	−81.285307	153.225085	1634.714	269.714	7.09	0.63	LW1 Nunatak	Sandstone	Cobble	Perched on bedrock platform
OT02	−81.285372	153.225027	1632.385	267.385	8.04	0.79	LW1 Nunatak	Gneiss	Cobble	Perched on bedrock platform
OT03	−81.285362	153.225665	1634.338	269.338	8.44	0.78	LW1 Nunatak	Sandstone	Cobble	Perched on bedrock platform
OT04A	−81.28521	153.221907	1629.108	264.108	8.05	0.72	LW1 Nunatak	Granite	Cobble	Perched on bedrock platform
OT05A	−81.2841	153.223108	1611.366	246.366	7.00	0.62	LW1 Nunatak	Sandstone	Cobble	Perched on bedrock platform
OT05C	−81.2841	153.223108	1611.366	246.366	7.59	0.68	LW1 Nunatak	Sandstone	Cobble	Perched on bedrock platform
OT07	−81.283113	153.221711	1602.697	237.697	6.95	0.61	LW1 Nunatak	Sandstone	Cobble	Perched on bedrock at break in slope
OT08	−81.282989	153.223401	1595.895	230.895	69.57	6.44	LW1 Nunatak	Sandstone	Cobble	Perched on bedrock near at break in slope
OT09	−81.28271	153.224258	1579.55	214.55	7.70	0.71	LW1 Nunatak	Sandstone	Cobble	Perched on bedrock on slope
OT10	−81.282584	153.225129	1569.281	204.281	8.12	0.75	LW1 Nunatak	Gneiss	Cobble	Perched on bedrock on slope
OT12	−81.282293	153.227478	1542.506	177.506	63.55	5.88	LW1 Nunatak	Sandstone	Cobble	Perched on bedrock on slope
OT13	−81.28215	153.22865	1527.657	162.657	57.85	5.59	LW1 Nunatak	Quartzite	Cobble	Perched on bedrock on slope
OT14A	−81.281456	153.233126	1484.729	119.729	6.41	0.59	LW1 Nunatak	Sandstone	Cobble	Perched on bedrock on slope
OT15	−81.281141	153.235754	1460.355	95.355	6.28	0.59	LW1 Nunatak	Gneiss	Cobble	Perched on bedrock on slope
OT17	−81.280698	153.242471	1418	53	5.50	0.52	LW1 Nunatak	Sandstone	Cobble	Perched on bedrock on slope
OT18	−81.28015	153.247993	1392	27	37.63	3.43	LW1 Nunatak	Quartzite	Cobble	Perched on bedrock on slope
GPS01A	−81.346045	152.729507	1594.664	114.664	3.60	0.34	GPS Nunatak	Sandstone	Cobble	Perched on bedrock
GPS02C	−81.346038	152.730276	1588.701	108.701	31.61	2.90	GPS Nunatak	Sandstone	Cobble	Perched on bedrock
GPS03C	−81.345982	152.731101	1585.117	105.117	7.03	0.63	GPS Nunatak	Sandstone	Cobble	Perched on bedrock
T01A	−81.357061	152.760153	1671.72	191.72	15.02	1.37	Tiger Nunatak	Sandstone	Cobble	Perched on bedrock platform
T01C	−81.357061	152.760153	1671.72	191.72	14.80	1.68	Tiger Nunatak	Granite	Cobble	Perched on bedrock platform
T01D	−81.357061	152.760153	1671.72	191.72	15.92	1.81	Tiger Nunatak	Quartzite	Cobble	Perched on bedrock platform
T02	−81.355038	152.75666	1663.72	183.72	5.59	0.52	Tiger Nunatak	Gneiss	Cobble	Perched on bedrock platform
LW2BP	−81.341	152.679	1487	7	27.97	2.34	LW2 Nunatak	Quartzite	Cobble	Resting on moraine surface
LW2Ro	−81.341	152.679	1487	7	2.56	0.27	LW2 Nunatak	Granite	Cobble	Resting on moraine surface
LW215	−81.341	152.679	1487	7	25.20	2.11	LW2 Nunatak	Quartzite	Cobble	Resting on moraine surface
R3-5	−80.501827	158.72932	306	261	24.20	2.35	Mt. Tadpole	Granite	Cobble	Perched on bedrock
R3-6	−80.501827	158.72932	306	261	7.92	0.94	Mt. Tadpole	Granite	Cobble	Perched on bedrock

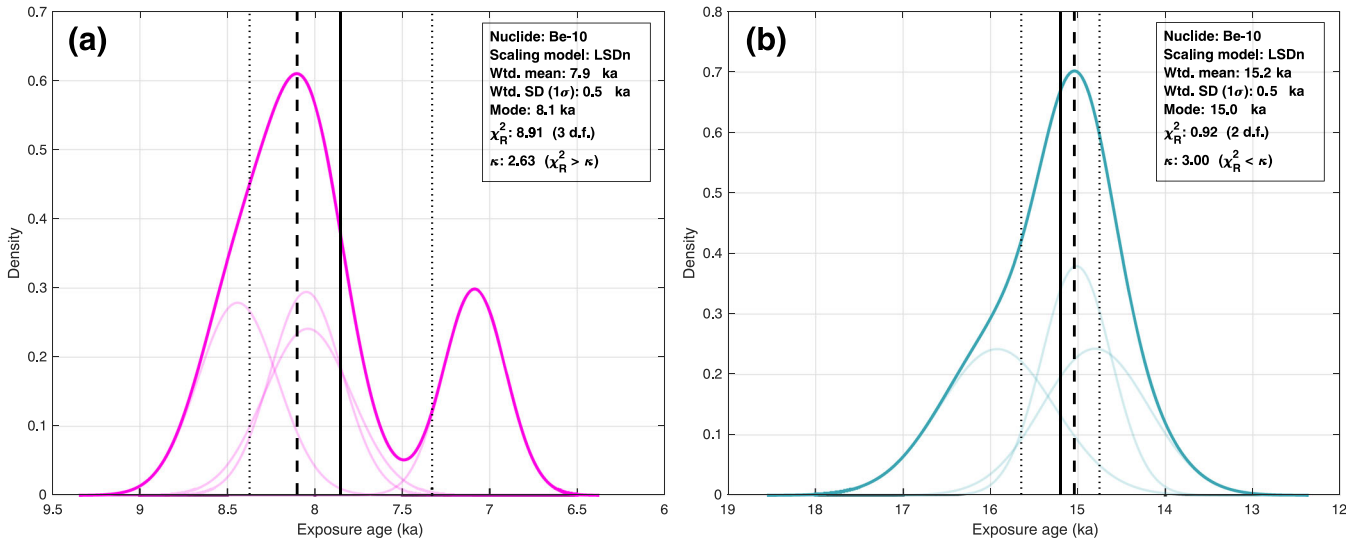

FIGURE 5 Kernel density estimate plots (Jones et al., 2019) for (a) four samples taken from broad plateau of LW1 with weighted mean exposure age of 7.85 ± 0.5 ka and interpreted to track initial thinning at LW1 Nunatak and (b) three samples taken from highest sampling location of the Lonewolf Nunataks (Tiger Nunatak) indicating a weighted mean exposure age of 15.2 ± 0.5 ka and interpreted to represent initial thinning of the Lonewolf Nunataks following the Last Glacial Maximum.

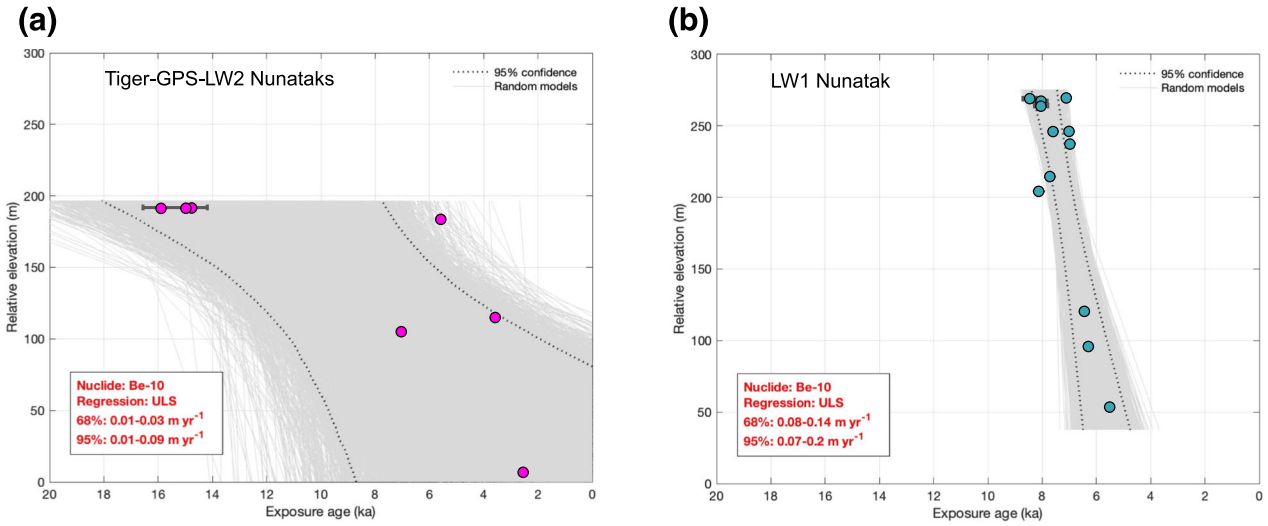

FIGURE 6 Paleo-thinning profiles and rates (Jones et al., 2019) for (a) transect 2 for all ages <20 ka, (b) transect 1 for all ages <20 ka.

lowest elevation samples ($n = 3$) found at 1487 m.a.s.l are erratic cobbles from moraine deposit (Palmer et al., 2012) perched seven metres above the modern Byrd Glacier and show a wide range of ages from ~28–25 to 2.6 ka. We interpret the youngest exposure age to represent the level of the ice surface at 2.6 ka while the two other samples may contain inherited inventories of cosmogenic nuclides from prior exposure.

3.3 | Mt. Tadpole

Two granitic erratic samples were collected ~250 m above the modern Byrd Glacier at Mt. Tadpole, a site of exposed bedrock along the southern Byrd Fiord (Figures 3c and S3). Calculated exposure ages are 24.2 ± 2.6 and 7.9 ± 0.9 ka. Here, we interpret the older age to represent inheritance from prior exposure/burial while the younger age coincides with the thinning seen in the LW1 Nunatak record.

3.4 | Paleo-thinning rates

Paleo-thinning rates are a useful measure of past ice sheet change for comparison with other records around Antarctica, while also providing assessments of modelled paleo-thinning rates and modern satellite-based thinning estimates (Small et al., 2019). Using Transect 2 samples and the 'estimate linear thinning rate' tool (Jones et al., 2019), the thinning rate for Tiger-GPS Nunataks is 0.01–0.03 m/year (68% confidence) and 0.01–0.09 m/year (95% confidence) (Figure 6a). For Transect 1, we determine a thinning rate of 0.08–0.14 (68% confidence) and 0.07–0.2 m/year (95% confidence) (Figure 6b). Paleo-thinning records from inland East Antarctic sites are rare, but a record from Mt. Kring along the upper David Glacier (Figure 1a) shows a paleo-thinning rate of 0.07–0.12 m/year (68% confidence) and 0.06–0.19 m/year (95% confidence) (Stutz et al., 2021), similar to Holocene paleo-thinning calculated for Transect 1 of this study.

4 | DISCUSSION

4.1 | Variable thinning along Lonewolf Nunataks

While complex ice flow around nunataks and the impact on inventories of cosmogenic nuclides has been suggested previously (Sugden et al., 2005), this new record from Lonewolf Nunataks and recent ice flow modelling (Mas E Braga et al., 2021) represent an additional improvement in understanding processes involving localised ice-topography interactions. Ice flow modelling (Mas E Braga et al., 2021) suggests that in scenarios where nunataks are oriented parallel to ice flow (e.g., Lonewolf Nunataks), we should expect to observe slower, earlier thinning in the upstream portions of the nunatak compared with the downstream portions (Mas E Braga et al., 2021), which is consistent with our results from Transects 1 and 2. This ice flow modelling, together with the observed strong topographic relief of Lonewolf Nunataks and variable thinning histories, provides an explanation for differences in ice thinning timing and style (Figure 4). Local differences observed in this study and supported by ice flow modelling using a locally refined grid are not typically demonstrated in coarser ice sheet models and may explain the common timing gap between paleo-thinning records and ice sheet models (Johnson et al., 2021; Jones et al., 2020; Stutz et al., 2021).

4.2 | Data-model comparison

The timing and rates of modelled ice thickness changes since the LGM at Lonewolf Nunataks vary greatly between models and key model parameters (Figure 7). Model ensemble A exhibits local ice thicknesses of 200–900 m greater than present for the LGM. Of the model parameters, ESIA, which is used to account for ice dynamical uncertainty, exhibits the most influence on LGM ice thickness of Byrd Glacier. The relationship between ice thickness and ESIA is nonlinear, with an intermediate value producing the lowest ice sheet thickness. In terms of the timing of deglacial ice thinning at Byrd, ESSA, which controls ice sheet sliding in grounded ice regions, has the most significant impact of the parameters. Lower values of ESSA, which produce slower and thicker ice streams, yield a thicker LGM ice sheet and later deglacial ice thinning.

Model ensemble B exhibits a narrower range of LGM thickness anomalies that span 200–400 m greater than present (Figure 7b). The model ensemble B simulations group according to variations in the basal sliding coefficient (CSHELF) applied to grounded ice on the modern seafloor, with values that promote greater sliding rates resulting in thinner ice and vice versa. Simulations using the fastest sliding coefficient produce a close match with the ca. 15-ka initial constraints from Tiger Nunatak but do not provide a good fit to the rest of the record from Lonewolf Nunataks.

Despite wide variability in the modelled LGM ice thickness at Lonewolf Nunataks, most simulations across both models predict that ice thinning occurred in a single step of thinning. In model ensemble A, the timing of this single step thinning varies noticeably between simulations. The ensemble mean onset of thinning events of 13.2 ± 1.3 ka (±1.s.d) with a duration of 4.1 ± 1.0 ka. In contrast, model ensemble B simulations are relatively consistent across the parameter space, with thinning beginning 9.8 ± 0.4 ka and lasting 1.8 ± 0.4 ka. These simulations support a conceptual model of progressive southward grounding line retreat following the LGM (Lowry et al., 2019).

In both model ensembles, the timing of this thinning at Lonewolf Nunataks precedes that recorded in the LW1 sample set by several millennia (Figure 7). Only one model run (model ensemble set A; ESSA = 0.4) produces an ice thickness anomaly curve that closely matches the timing as recorded in the LW1 Nunatak samples, however this simulation predicts an LGM and early deglacial ice thickness that exceeds the 15-ka constraint from Tiger Nunatak by ~600 m (Figure 7a).

Despite the mismatch in ice thickness at 15 ka and early onset of thinning relative to the geological constraints, the modelled rates of thinning at Lonewolf Nunataks are broadly comparable with those derived from our cosmogenic constraints. Both model ensembles are

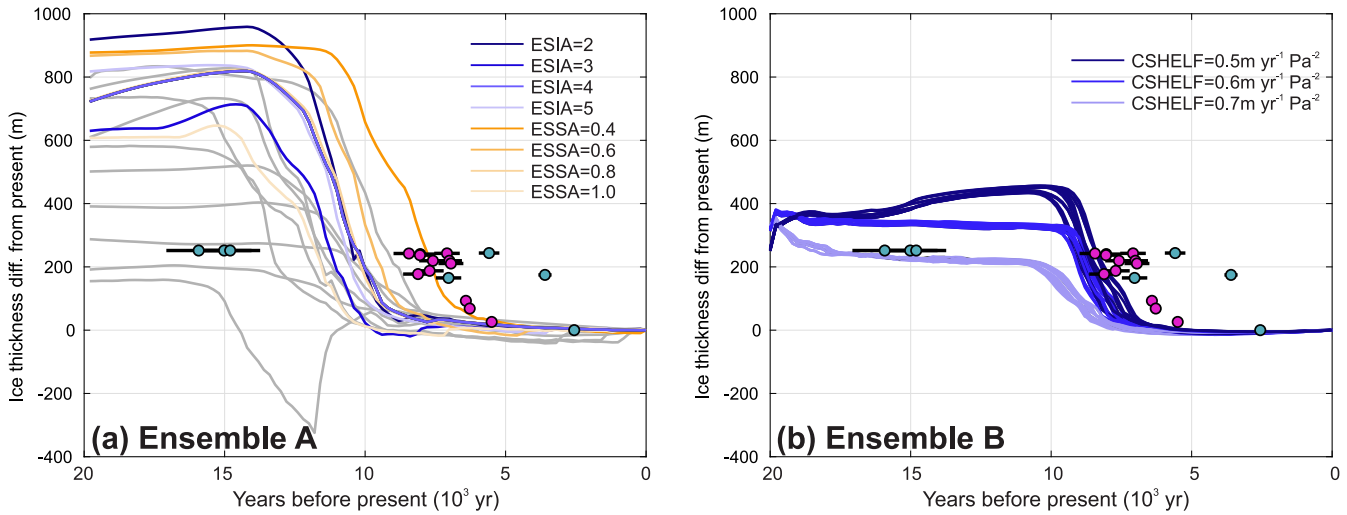

FIGURE 7 Modelled ice thickness at Lonewolf Nunataks as simulated by the model ensemble A (panel a; Lowry et al., 2019, 2020) and model ensemble B (panel b; Hillebrand et al., 2021). In panel (a), the ESIA and ESSA sensitivity experiments are distinguished to support the written discussion, whereas outputs for other experiments (see Methods for full description) are uniformly grey. Identical in both panels are cosmogenic ^{10}Be ages from Transect 1 (magenta) and Transect 2 (cyan).

TABLE 5 The timing, magnitude and rate of ice surface lowering at Lonewolf Nunataks, Byrd Glacier as simulated in in two transient deglacial ice sheet model ensembles (A: Lowry et al., 2019, 2020; and B: Hillebrand et al., 2021).

Experiment	Onset (ka)	End (ka)	Duration (year)	onsetH (m)	onset_dH(m)	endingH (m)	ending_dH(m)	modernH (m)	Thin-mag (m)	Thin-rate (m/year)
Model ensemble A										
ESIA2	−13 200	−8800	4400	1924	922	1031	29	1002	−893	−0.20
ESIA3	−14 000	−9600	4400	1756	694	1056	−6	1062	−700	−0.16
ESIA4	−13 400	−9200	4200	1801	789	1083	71	1011	−718	−0.17
ESIA5	−13 800	−9600	4200	1764	811	1019	66	953	−745	−0.18
ESSA0.4	−11 000	−6200	4800	1710	855	900	45	854	−810	−0.17
ESSA0.6	−12 000	−7800	4200	1755	811	981	36	944	−775	−0.18
ESSA0.8	−13 400	−9200	4200	1801	789	1083	71	1011	−718	−0.17
ESSA1.0	−14 600	−10 400	4200	1667	622	1071	26	1045	−596	−0.14
MV1e18	−13 200	−9200	4000	1793	782	1078	68	1010	−714	−0.18
MV1e19	−13 400	−9200	4200	1801	789	1083	71	1011	−718	−0.17
MV1e20	−13 800	−8800	5000	1817	791	1048	22	1026	−769	−0.15
MV1e21	−11 400	−11 000	400	1724	120	1699	95	1604	−25	−0.06
climavg	−13 400	−9200	4200	1801	789	1083	71	1011	−718	−0.17
climcool	−11 800	−7800	4000	1736	749	1034	46	987	−703	−0.18
climwarm	−14 200	−9800	4400	1773	709	1087	24	1063	−685	−0.16
phi3	−15 600	−10 800	4800	1553	697	895	39	856	−658	−0.14
phi4	−15 200	−9200	6000	1562	116	1461	15	1446	−101	−0.02
phi6	−14 600	−10 400	4200	1535	526	1036	28	1008	−498	−0.12
phi9	−13 400	−9200	4200	1801	789	1083	71	1011	−718	−0.17
q0.25	−13 400	−9200	4200	1801	789	1083	71	1011	−718	−0.17
q0.5	−13 000	−9000	4000	1751	486	1323	58	1265	−428	−0.11
q0.75	−11 400	−8800	2600	1696	350	1420	74	1346	−277	−0.11
q1.0	−10 600	−7600	3000	1657	230	1466	39	1427	−192	−0.06
Mean	−13 209	−9130	4078	1738	653	1135	49	1086	−603	−0.15
StdDev	1311	1071	1021	93	235	199	25	194	236	0.05
Model ensemble B										
'LR04_tau1000_ocfac0_5_shelf5_calv0_7.nc'	−10 200	−8400	1800	908	177	766	36	731	−141	−0.08
'LR04_tau1000_ocfac0_5_shelf5_calv1.nc'	−10 200	−8600	1600	907	176	777	46	731	−130	−0.08
'LR04_tau1000_ocfac0_5_shelf6_calv0_7.nc'	−9400	−7600	1800	1023	286	771	34	737	−252	−0.14
'LR04_tau1000_ocfac0_5_shelf6_calv1.nc'	−9600	−7600	2000	1033	295	768	31	737	−264	−0.13
'LR04_tau1000_ocfac0_5_shelf7_calv1.nc'	−9800	−7000	2800	1205	414	829	38	791	−376	−0.13
'LR04_tau1000_ocfac1_shelf5_calv0_7.nc'	−10 400	−8600	1800	912	182	769	38	731	−143	−0.08

TABLE 5 (Continued)

Experiment	Onset (ka)	End (ka)	Duration (year)	onsetH (m)	onset_dH(m)	endingH (m)	ending_dH(m)	modernH (m)	Thin-mag (m)	Thin-rate (m/year)
'LR04_tau1000_ocfac1_shelf5_calv1.nc'	−10 600	−8800	1800	921	190	780	49	731	−141	−0.08
'LR04_tau1000_ocfac1_shelf6_calv0_7.nc'	−9600	−7800	1800	1022	287	758	23	735	−264	−0.15
'LR04_tau1000_ocfac1_shelf6_calv1.nc'	−9800	−7800	2000	1034	300	757	22	735	−278	−0.14
'LR04_tau1000_ocfac1_shelf7_calv0_7.nc'	−10 000	−7400	2600	1203	412	831	40	791	−372	−0.14
'LR04_tau1000_ocfac1_shelf7_calv1.nc'	−10 200	−7400	2800	1211	420	828	37	791	−383	−0.14
'LR04_tau2000_ocfac0_5_shelf5_calv0_7.nc'	−10 200	−8800	1400	914	185	795	66	729	−119	−0.08
'LR04_tau2000_ocfac0_5_shelf5_calv1.nc'	−10 000	−8800	1200	903	172	794	64	731	−108	−0.09
'LR04_tau2000_ocfac0_5_shelf6_calv0_7.nc'	−9400	−8000	1400	1038	295	798	56	742	−239	−0.17
'LR04_tau2000_ocfac0_5_shelf6_calv1.nc'	−9400	−8000	1400	1037	295	796	54	742	−241	−0.17
'LR04_tau2000_ocfac0_5_shelf7_calv0_7.nc'	−9800	−7800	2000	1207	407	869	69	800	−338	−0.17
'LR04_tau2000_ocfac0_5_shelf7_calv1.nc'	−9800	−7800	2000	1212	411	863	62	801	−349	−0.17
'LR04_tau2000_ocfac1_shelf5_calv0_7.nc'	−10 400	−9000	1400	920	191	807	79	729	−112	−0.08
'LR04_tau2000_ocfac1_shelf5_calv1.nc'	−10 400	−9000	1400	918	189	803	75	729	−115	−0.08
'LR04_tau2000_ocfac1_shelf6_calv0_7.nc'	−9600	−8200	1400	1036	296	791	51	740	−245	−0.18
'LR04_tau2000_ocfac1_shelf6_calv1.nc'	−9600	−8400	1200	1035	294	826	86	740	−208	−0.17
'LR04_tau2000_ocfac1_shelf7_calv0_7.nc'	−10 000	−8000	2000	1208	408	853	53	800	−355	−0.18
'LR04_tau2000_ocfac1_shelf7_calv1.nc'	−10 200	−8200	2000	1211	411	865	65	800	−346	−0.17
'SPRATT_tau1000_ocfac0_5_shelf5.nc'	−10 000	−8200	1800	920	192	774	47	728	−145	−0.08
'SPRATT_tau1000_ocfac0_5_shelf5_calv0_7.nc'	−9800	−8000	1800	911	183	760	32	728	−151	−0.08
'SPRATT_tau1000_ocfac0_5_shelf6.nc'	−9200	−7400	1800	1040	305	774	40	734	−266	−0.15
'SPRATT_tau1000_ocfac0_5_shelf6_calv0_7.nc'	−9200	−7400	1800	1039	305	777	42	734	−262	−0.15
'SPRATT_tau1000_ocfac0_5_shelf7.nc'	−9400	−7000	2400	1216	427	835	46	789	−381	−0.16
'SPRATT_tau1000_ocfac0_5_shelf7_calv0_7.nc'	−9400	−6800	2600	1214	424	824	34	790	−390	−0.15
'SPRATT_tau1000_ocfac1_shelf5.nc'	−10 200	−8200	2000	921	192	765	36	729	−157	−0.08
'SPRATT_tau1000_ocfac1_shelf5_calv0_7.nc'	−10 000	−8200	1800	915	186	767	38	729	−148	−0.08
'SPRATT_tau1000_ocfac1_shelf6.nc'	−9400	−7600	1800	1038	304	773	40	734	−264	−0.15
'SPRATT_tau1000_ocfac1_shelf6_calv0_7.nc'	−9400	−7600	1800	1042	308	775	41	734	−268	−0.15
'SPRATT_tau1000_ocfac1_shelf7.nc'	−9800	−7400	2400	1218	429	845	56	790	−373	−0.16
'SPRATT_tau1000_ocfac1_shelf7_calv0_7.nc'	−9800	−7400	2400	1222	432	848	58	790	−374	−0.16
'SPRATT_tau2000_ocfac0_5_shelf5.nc'	−10 000	−8200	1800	921	191	773	44	729	−147	−0.08
'SPRATT_tau2000_ocfac0_5_shelf5_calv0_7.nc'	−9800	−8400	1400	913	183	782	52	730	−131	−0.09
'SPRATT_tau2000_ocfac0_5_shelf6.nc'	−9200	−7800	1400	1039	299	801	61	740	−238	−0.17
'SPRATT_tau2000_ocfac0_5_shelf6_calv0_7.nc'	−9200	−7800	1400	1042	302	810	70	740	−232	−0.17

(Continues)

TABLE 5 (Continued)

Experiment	Onset (ka)	End (ka)	Duration (year)	onsetH (m)	onset_dH(m)	endingH (m)	ending_dH(m)	modernH (m)	Thin-mag (m)	Thin-rate (m/year)
'SPRATT_tau2000_ocfac0_5_shelf7.nc'	−9400	−7200	2200	1228	428	850	49	801	−378	−0.17
'SPRATT_tau2000_ocfac0_5_shelf7_calv0_7.nc'	−9400	−7400	2000	1231	431	856	56	800	−375	−0.19
'SPRATT_tau2000_ocfac1_shelf5.nc'	−10 200	−8400	1800	924	195	778	49	729	−146	−0.08
'SPRATT_tau2000_ocfac1_shelf5_calv0_7.nc'	−10 200	−8200	2000	926	197	769	39	730	−158	−0.08
'SPRATT_tau2000_ocfac1_shelf6.nc'	−9600	−8000	1600	1045	306	795	56	739	−250	−0.16
'SPRATT_tau2000_ocfac1_shelf6_calv0_7.nc'	−9400	−8000	1400	1040	304	802	67	735	−237	−0.17
'SPRATT_tau2000_ocfac1_shelf7.nc'	−9600	−8000	1600	1224	425	889	90	799	−335	−0.21
'SPRATT_tau2000_ocfac1_shelf7_calv0_7.nc'	−9600	−7400	2200	1226	427	847	47	799	−380	−0.17
Mean	−9783	−7936	1847	1053	299	804	50	753	−249	−0.13
StdDev	377	536	400	124	96	36	15	30	96	0.04

in good agreement with ensemble mean average thinning rates of 0.15 ± 0.05 m/year and 0.13 ± 0.04 m/year for A and B, respectively (Table 5).

4.3 | Inland thinning and grounding line retreat in Ross Embayment

Comparing the thinning history derived from Lonewolf Nunataks against those from regional ice sheet models, we link inland thinning to grounding line retreat in the Ross Sea. Modelled grounding line location varies between the two ensemble sets yet all retreat and modelled thinning happens during one event. A single, abrupt thinning event is also recorded in adjacent TAM outlet glacier thinning records south of Northern Victoria Land (including David, Mawson, Mackay, Darwin-Hatherton, Beardmore, Shackleton, Scott and Reedy Glaciers) suggesting a western Ross Sea trend in abrupt thinning initiating or underway between ~9 and 8 ka (Hillebrand et al., 2021; Jones et al., 2015, 2020; King et al., 2020; Spector et al., 2017; Stutz et al., 2021) (Figure 8). The timing of grounding line retreat during this time comes from submarine mapping, sedimentary core analysis and bulk and foraminifera radiocarbon dating from post-LGM sediments (Domack et al., 1999; Lee et al., 2017; R. M. McKay et al., 2008; Prothro et al., 2020; Shipp et al., 1999). Immediately east of Ross Island and along a prominent Byrd Glacier flow path, open marine conditions were established by 8.6 ka near the modern-day calving line of the Ross Ice Shelf (R. McKay et al., 2016).

Most thinning records, constrained by surface exposure dating, from southern TAM outlet glaciers are located near the coastal outlet where greater ice thickness change and rapid ice thinning is expected as grounding lines retreated inside the fiords. In contrast, the Byrd Glacier is significantly larger, in terms of ice discharge and overall drainage area, than all other southern TAM glaciers combined. The large scale of the Byrd Glacier, together with its gentle inland topography, suggests inland thinning can reach further inland than other nearby outlet glaciers, which exhibit relatively steep elevation profiles immediately upstream from the modern grounding line (Felikson et al., 2017, 2021) (Figure 9). This inland reach of ice mass loss implies that the Byrd Glacier can contribute much more to sea level rise. Additionally, in situ measured extreme basal melt at the ice shelf front (Stewart et al., 2019) could initiate an increase in velocity reaching as far as the Lonewolf Nunataks, a future scenario which could force a grounding line retreat of the Byrd Glacier to a prominent stable ridge upstream of its current position (Morlighem et al., 2020; Reese et al., 2018; Stearns et al., 2008).

Taken together, our data-ice sheet model analysis supports a progressive southward grounding line retreat initiated during the early Holocene and associated with rapid inland thinning (Figure 2). Notably both model ensembles exhibit the most rapid thinning following ice shelf formation. Such a connection between basal sliding and downstream shifts in glacial extent are supported by recent studies of uplifted subglacial precipitates. These studies highlight a strong coupling between climate-regulated ice sheet variances in the Ross Sea and basal freeze-flush cycles within TAM outlet glaciers (Blackburn et al., 2020; Piccione et al., 2022).

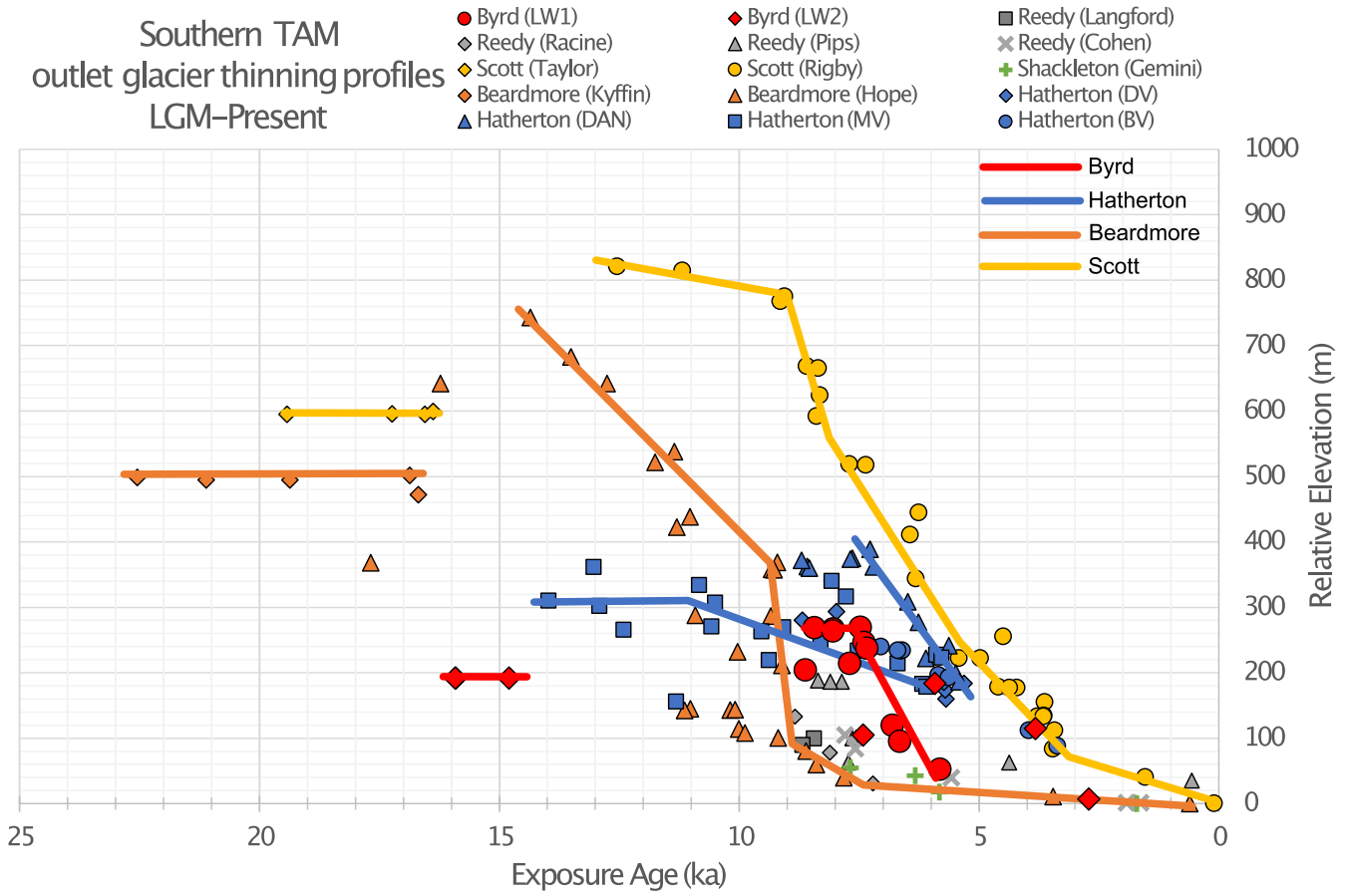

FIGURE 8 Surface exposure age data and generalised interpretation trends from this study and three other glaciers along the TAM (Hillebrand et al., 2021; King et al., 2020; Spector et al., 2017) showing local variation but broad agreement in constraining an early Holocene pulse of abrupt thinning. Data from Reedy (Todd et al., 2010) and Shackleton (Spector et al., 2017) glaciers included without generalised trends due to limited data.

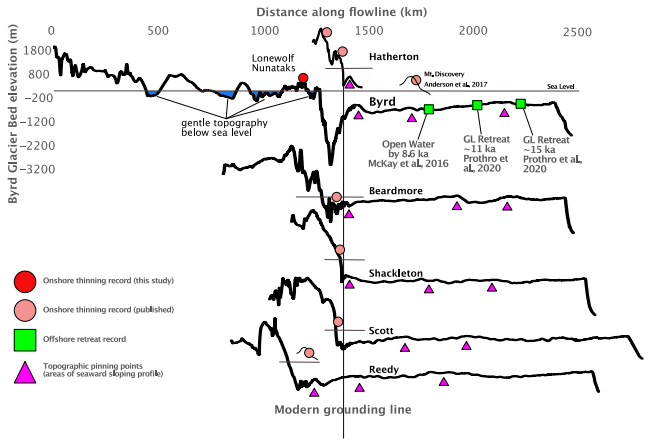

FIGURE 9 Bed profiles for selected glaciers of the Southern TAM. Bed profiles derived from BedMachine (Morlighem et al., 2020), modern (Rignot et al., 2011) and modelled paleo-ice surface velocity (Whitehouse et al., 2012). Flowline locations are shown in Figure 1a. All bed profiles are on same scale and vertically shifted for visibility and horizontally aligned at the modern grounding lines for each glacier. Sea level projected as thin grey line delimits upstream areas which lie below sea level. Onshore and offshore constraints projected to location along respective flowline. Mt. Discovery surface profile and onshore constraints (Anderson et al., 2017) projected on Byrd Flowline.

5 | CONCLUSIONS

In this study, we use glacial erratic cobbles to provide new inland paleo-thinning constraints for the Byrd Glacier, one of the largest glaciers on Earth. We close a significant spatial and temporal gap in past AIS reconstruction by constraining the upper Byrd Glacier's thinning history from ~15 to 2 ka. Its thinning history broadly overlaps with paleo-thinning records from nearby TAM outlet glaciers with some variation in onset of thinning, potentially due to local factors related to complex topography near the TAM. Rapid ice thinning at ~9–8 ka in nearly all available records demonstrates the regional, single-step ice thinning signal related to grounding line retreat throughout the Ross Embayment. Our data-model comparison demonstrates that inland thinning extends 100s km from perturbations at the grounding line and ice shelf front and is linked to temporal changes in the basal sliding regime.

AUTHOR CONTRIBUTIONS

Jamey Stutz: Conceptualization; funding acquisition; methodology; investigation; resources; software; supervision; writing—original draft; writing—review/editing. **Shaun Eaves**: Conceptualization; funding acquisition; methodology; investigation; resources; software; supervision; writing—original draft; writing—review/editing. **Kevin Norton**:

Conceptualization; funding acquisition; methodology; resources; supervision; writing—original draft; writing—review/editing. **Klaus M. Wilcken**: Methodology; investigation; resources; writing—review/editing. **Claudia Moore**: Methodology; writing—review/editing. **Rob McKay**: Funding acquisition; investigation; resources; supervision; writing—review/editing. **Dan Lowry**: Conceptualization; methodology; writing—original draft; writing—review/editing. **Kathy Licht**: Methodology; resources; writing—review/editing. **Katelyn Johnson**: Conceptualization; methodology; writing—original draft; writing—review/editing.

ACKNOWLEDGEMENTS

This project would not be possible without the work of many individuals of the, Antarctica New Zealand, U. S Antarctic Program, Crew and pilots of New Zealand Defence Force, Kenn Borek Air, Ltd, and the 109th Airlift Wing of the New York Air National Guard. This work is part of Project 1, Objective 1 of the Antarctic Science Platform, funded by the New Zealand Ministry of Business, Innovation and Employment. We received helpful field logistics and safety information from POLENET scientists Terry Wilson and Dave Saddler. We acknowledge the Antarctic Research Centre, School of Geography, Earth and Environmental Sciences at Te Herenga Waka - Victoria University of Wellington for lasting support of this project. We acknowledge the financial support to Centre for Accelerator Science (CAS) at Australian Nuclear Sciences and Technology Organisation (ANSTO) by the National Collaborative Research Infrastructure Strategy (NCRIS). This work was part of ANSTO research grant AP12721 and Australian Institute of Nuclear Sciences Early Career Researcher Grant awarded to JS. All authors declare there are no conflicts of interest with this work. Open access publishing facilitated by Victoria University of Wellington, as part of the Wiley - Victoria University of Wellington agreement via the Council of Australian University Librarians.

DATA AVAILABILITY STATEMENT

All data for this study that have not previously been published are included in Tables 1–5 and are available on the informal cosmogenic nuclide exposure age database https://version2.ice-d.org/.

ORCID

Jamey Stutz https://orcid.org/0000-0002-5645-3311

REFERENCES

Anderson, J.B., Conway, H., Bart, P.J., Witus, A.E., Greenwood, S.L., McKay, R.M., et al. (2014) Ross Sea paleo-ice sheet drainage and deglacial history during and since the LGM. *Quaternary Science Reviews*, 100, 31–54. Available from: https://doi.org/10.1016/j.quascirev.2013.08.020

Anderson, J.T.H., Wilson, G.S., Fink, D., Lilly, K., Levy, R.H. & Townsend, D. (2017) Reconciling marine and terrestrial evidence for post LGM ice sheet retreat in southern McMurdo Sound, Antarctica. *Quaternary Science Reviews*, 157, 1–13. Available from: https://doi.org/10.1016/j.quascirev.2016.12.007

Balco, G. (2011) Contributions and unrealized potential contributions of cosmogenic-nuclide exposure dating to glacier chronology, 1990–2010. *Quaternary Science Reviews*, 30(1), 3–27. Available from: https://doi.org/10.1016/j.quascirev.2010.11.003

Balco, G., Stone, J.O., Lifton, N.A. & Dunai, T.J. (2008) A complete and easily accessible means of calculating surface exposure ages or erosion rates from ^{10}Be and ^{26}Al measurements. *Quaternary Geochronology*, 3(3), 174–195. Available from: https://doi.org/10.1016/J.QUAGEO.2007.12.001

Bart, P.J., DeCesare, M., Rosenheim, B.E., Majewski, W. & McGlannan, A. (2018) A centuries-long delay between a paleo-ice-shelf collapse and grounding-line retreat in the Whales Deep Basin, eastern Ross Sea, Antarctica. *Scientific Reports*, 8(1), 12392. Available from: https://doi.org/10.1038/s41598-018-29911-8

Bentley, M.J., Ó Cofaigh, C., Anderson, J.B., Conway, H., Davies, B., Graham, A.G.C., et al. (2014) A community-based geological reconstruction of Antarctic Ice Sheet deglaciation since the Last Glacial Maximum. *Quaternary Science Reviews*, 100, 1–9. Available from: https://doi.org/10.1016/j.quascirev.2014.06.025

Bindschadler, R., Vornberger, P., Fleming, A., Fox, A., Mullins, J., Binnie, D., et al. (2008) The Landsat image mosaic of Antarctica. *Remote Sensing of Environment*, 112(12), 4214–4226. Available from: https://doi.org/10.1016/j.rse.2008.07.006

Blackburn, T., Edwards, G.H., Tulaczyk, S., Scudder, M., Piccione, G., Hallet, B., et al. (2020) Ice retreat in Wilkes Basin of East Antarctica during a warm interglacial. *Nature*, 583(7817), 554–559. Available from: https://doi.org/10.1038/s41586-020-2484-5

Bueler, E. & Brown, J. (2009) Shallow shelf approximation as a "sliding law" in a thermomechanically coupled ice sheet model. *Journal of Geophysical Research*, 114(F3), F03008. Available from: https://doi.org/10.1029/2008JF001179

Chambers, C., Greve, R., Obase, T., Saito, F. & Abe-Ouchi, A. (2022) Mass loss of the Antarctic ice sheet until the year 3000 under a sustained late-21st-century climate. *Journal of Glaciology*, 68(269), 605–617. Available from: https://doi.org/10.1017/JOG.2021.124

Conway, H., Hall, B.L., Denton, G.H., Gades, A.M. & Waddington, E.D. (1999) Past and future grounding-line retreat of the West Antarctic Ice Sheet. *Science (New York, N.Y.)*, 286(5438), 280–283. Available from: https://doi.org/10.1126/science.286.5438.280

Cuffey, K.M., Clow, G.D., Steig, E.J., Buizert, C., Fudge, T.J., Koutnik, M., et al. (2016) Deglacial temperature history of West Antarctica. *Proceedings of the National Academy of Sciences of the United States of America*, 113(50), 14249–14254. Available from: https://doi.org/10.1073/pnas.1609132113

Das, I., Padman, L., Bell, R.E., Fricker, H.A., Tinto, K.J., Hulbe, C.L., et al. (2020) Multidecadal basal melt rates and structure of the Ross Ice Shelf, Antarctica, using airborne ice penetrating radar. *Journal of Geophysical Research - Earth Surface*, 125(3), e2019JF005241. Available from: https://doi.org/10.1029/2019JF005241

DeConto, R.M. & Pollard, D. (2016) Contribution of Antarctica to past and future sea-level rise. *Nature*, 531(7596), 591–597. Available from: https://doi.org/10.1038/nature17145

Domack, E.W., Jacobson, E.A., Shipp, S. & Anderson, J.B. (1999) Late Pleistocene–Holocene retreat of the West Antarctic Ice-Sheet system in the Ross Sea: part 2—sedimentologic and stratigraphic signature. *Geological Society of America Bulletin*, 111(10), 1517–1536. Available from: https://doi.org/10.1130/0016-7606(1999)111<1517:LPHROT>2.3.CO;2

Elderfield, H., Ferretti, P., Greaves, M., Crowhurst, S., McCave, I.N., Hodell, D., et al. (2012) Evolution of ocean temperature and ice volume through the mid-Pleistocene climate transition. *Science*, 337(6095), 704–709. Available from: https://doi.org/10.1126/science.1221294

Felikson, D., Bartholomaus, T.C., Catania, G.A., Korsgaard, N.J., Kjær, K.H., Morlighem, M., et al. (2017) Inland thinning on the Greenland ice sheet controlled by outlet glacier geometry. *Nature Geoscience*, 10(5), 366–369. Available from: https://doi.org/10.1038/ngeo2934

Felikson, D., Catania, G., Bartholomaus, T.C., Morlighem, M. & Noël, B.P.Y. (2021) Steep glacier bed knickpoints mitigate inland thinning in Greenland. *Geophysical Research Letters*, 48(2), e2020GL090112. Available from: https://doi.org/10.1029/2020GL090112

Fox-Kemper, B., Hewitt, H. T., Xiao, C., Aðalgeirsdóttir, G., Drijfhout, S. S., Edwards, T. L., Golledge, N. R., Hemer, M., Kopp, R. E., Krinner, G., Mix, A., Notz, D., Nowicki, S., Nurhati, I. S., Ruiz, L., Sallée, J. B., Slangen, A. B. A., & Yu, Y. (2021). Ocean, Cryosphere and Sea Level Change. In Climate Change 2021: The Physical Science Basis.

Contribution of Working Group I to the Sixth Assessment Report of the Intergovernmental Panel on Climate Change.

Fürst, J.J., Durand, G., Gillet-Chaulet, F., Tavard, L., Rankl, M., Braun, M., et al. (2016) The safety band of Antarctic ice shelves. *Nature Climate Change*, 6(5), 479–482. Available from: https://doi.org/10.1038/nclimate2912

Golledge, N.R., Kowalewski, D.E., Naish, T.R., Levy, R.H., Fogwill, C.J. & Gasson, E.G.W. (2015) The multi-millennial Antarctic commitment to future sea-level rise. *Nature*, 526(7573), 421–425. Available from: https://doi.org/10.1038/nature15706

Halberstadt, A.R.W., Simkins, L.M., Greenwood, S.L. & Anderson, J.B. (2016) Past ice-sheet behaviour: retreat scenarios and changing controls in the Ross Sea, Antarctica. *The Cryosphere*, 10, 1003–1020. Available from: https://doi.org/10.5194/tc-10-1003-2016

Hillebrand, T.R., Stone, J.O., Koutnik, M., King, C., Conway, H., Hall, B., et al. (2021) Holocene thinning of Darwin and Hatherton glaciers, Antarctica, and implications for grounding-line retreat in the Ross Sea. *The Cryosphere*, 15(7), 3329–3354. Available from: https://doi.org/10.5194/TC-15-3329-2021

Howat, I.M., Porter, C., Smith, B.E., Noh, M.-J. & Morin, P. (2019) The reference elevation model of Antarctica. *The Cryosphere*, 13(2), 665–674. Available from: https://doi.org/10.5194/tc-13-665-2019

Imbie, T. (2018) Mass balance of the Antarctic Ice Sheet from 1992 to 2017. *Nature*, 558(7709), 219–222. Available from: https://doi.org/10.1038/s41586-018-0179-y

Johnson, J.S., Pollard, D., Whitehouse, P.L., Roberts, S.J., Rood, D.H. & Schaefer, J.M. (2021) Comparing glacial-geological evidence and model simulations of ice sheet change since the last glacial period in the Amundsen Sea Sector of Antarctica. *Journal of Geophysical Research - Earth Surface*, 126(6), e2020JF005827. Available from: https://doi.org/10.1029/2020JF005827

Johnson, J.S., Venturelli, R.A., Balco, G., Allen, C.S., Braddock, S., Campbell, S., et al. (2022) Review article: existing and potential evidence for Holocene grounding line retreat and readvance in Antarctica. *The Cryosphere*, 16(5), 1543–1562. Available from: https://doi.org/10.5194/tc-16-1543-2022

Jones, R.S., Mackintosh, A.N., Norton, K.P., Golledge, N.R., Fogwill, C.J., Kubik, P.W., et al. (2015) Rapid Holocene thinning of an East Antarctic outlet glacier driven by marine ice sheet instability. *Nature Communications*, 6(1), 1–9. Available from: https://doi.org/10.1038/ncomms9910

Jones, R.S., Small, D., Cahill, N., Bentley, M.J. & Whitehouse, P.L. (2019) iceTEA: tools for plotting and analysing cosmogenic-nuclide surface-exposure data from former ice margins. *Quaternary Geochronology*, 51, 72–86. Available from: https://doi.org/10.1016/J.QUAGEO.2019.01.001

Jones, R.S., Whitmore, R.J., Mackintosh, A.N., Norton, K.P., Eaves, S.R., Stutz, J., et al. (2020) Regional-scale abrupt mid-Holocene ice sheet thinning in the western Ross Sea, Antarctica. *Geology*, 49(3), 278–282. Available from: https://doi.org/10.1130/g48347.1

Joughin, I., Smith, B.E. & Medley, B. (2014) Marine ice sheet collapse potentially under way for the Thwaites Glacier Basin, West Antarctica. *Science*, 344(6185), 735–738. Available from: https://doi.org/10.1126/science.1249055

King, C., Hall, B., Hillebrand, T. & Stone, J. (2020) Delayed maximum and recession of an East Antarctic outlet glacier. *Geology*, 48(6), 630–634. Available from: https://doi.org/10.1130/g47297.1

Kingslake, J., Scherer, R.P., Albrecht, T., Coenen, J., Powell, R.D., Reese, R., et al. (2018) Extensive retreat and re-advance of the West Antarctic Ice Sheet during the Holocene. *Nature*, 558(7710), 430–434. Available from: https://doi.org/10.1038/s41586-018-0208-x

Lee, J.I., McKay, R.M., Golledge, N.R., Yoon, H.I., Yoo, K.-C., Kim, H.J., et al. (2017) Widespread persistence of expanded East Antarctic glaciers in the southwest Ross Sea during the last deglaciation. *Geology*, 45(5), 403–406. Available from: https://doi.org/10.1130/G38715.1

Licht, K.J. & Palmer, E.F. (2013) Erosion and transport by Byrd Glacier, Antarctica during the Last Glacial Maximum. *Quaternary Science Reviews*, 62, 32–48. Available from: https://doi.org/10.1016/j.quascirev

Lifton, N., Sato, T. & Dunai, T.J. (2014) Scaling in situ cosmogenic nuclide production rates using analytical approximations to atmospheric cosmic-ray fluxes. *Earth and Planetary Science Letters*, 386, 149–160. Available from: https://doi.org/10.1016/J.EPSL.2013.10.052

Lingle, C.S. & Clark, J.A. (1985) A numerical model of interactions between a marine ice sheet and the solid earth: application to a West Antarctic ice stream. *Journal of Geophysical Research*, 90(C1), 1100. Available from: https://doi.org/10.1029/JC090iC01p01100

Lisiecki, L.E. & Raymo, M.E. (2005) A Pliocene-Pleistocene stack of 57 globally distributed benthic $\delta^{18}O$ records. *Paleoceanography*, 20(1) 2004PA001071, Available from: https://doi.org/10.1029/2004PA001071

Lisiecki, L.E. & Stern, J.V. (2016) Regional and global benthic $\delta^{18}O$ stacks for the last glacial cycle. *Paleoceanography*, 31(10), 1368–1394. Available from: https://doi.org/10.1002/2016PA003002

Liu, Z., Otto-Bliesner, B.L., He, F., Brady, E.C., Tomas, R., Clark, P.U., et al. (2009) Transient simulation of last deglaciation with a new mechanism for bolling-allerod warming. *Science*, 325(5938), 310–314. Available from: https://doi.org/10.1126/science.1171041

Lowry, D.P., Golledge, N.R., Bertler, N.A.N., Jones, R.S., McKay, R. & Stutz, J. (2020) Geologic controls on ice sheet sensitivity to deglacial climate forcing in the Ross Embayment, Antarctica. *Quaternary Science Advances*, 1, 100002. Available from: https://doi.org/10.1016/J.QSA.2020.100002

Lowry, D.P., Golledge, N.R., Bertler, N.A.N., Selwyn Jones, R. & McKay, R. (2019) Deglacial grounding-line retreat in the Ross Embayment, Antarctica, controlled by ocean and atmosphere forcing. *Science Advances*, 5(8), eaav8754. Available from: https://doi.org/10.1126/sciadv.aav8754

Mas e Braga, M., Selwyn Jones, R., Newall, J.C.H., Rogozhina, I., Andersen, J.L., Lifton, N.A., et al. (2021) Nunataks as barriers to ice flow: implications for palaeo ice sheet reconstructions. *The Cryosphere*, 15(10), 4929–4947. Available from: https://doi.org/10.5194/tc-15-4929-2021

McKay, R., Golledge, N.R., Maas, S., Naish, T., Levy, R., Dunbar, G., et al. (2016) Antarctic marine ice-sheet retreat in the Ross Sea during the early Holocene. *Geology*, 44(1), 7–10. Available from: https://doi.org/10.1130/G37315.1

McKay, R.M., Dunbar, G.B., Naish, T.R., Barrett, P.J., Carter, L. & Harper, M. (2008) Retreat history of the Ross Ice Sheet (Shelf) since the Last Glacial Maximum from deep-basin sediment cores around Ross Island. *Palaeogeography, Palaeoclimatology, Palaeoecology*, 260, 245–261. Available from: https://doi.org/10.1016/j.palaeo.2007.08.015

Menviel, L., Timmermann, A., Timm, O.E. & Mouchet, A. (2011) Deconstructing the Last Glacial termination: the role of millennial and orbital-scale forcings. *Quaternary Science Reviews*, 30(9–10), 1155–1172. Available from: https://doi.org/10.1016/j.quascirev.2011.02.005

Meredith, M., Sommerkorn, M., Cassotta, S., Derksen, C., Ekaykin, A., Hollowed, A., et al. (2019) Polar regions. In: Pörtner, H.-O., Roberts, D.C., MassonDelmotte, V., Zhai, P., Tignor, M., Poloczanska, E., *et al.* (Eds.) *IPCC special report on the ocean and cryosphere in a changing climate*. Cambridge, UK and New York, NY, USA: Cambridge University Press, pp. 203–320. Available from: https://doi.org/10.1017/9781009157964.005

Morlighem, M., Rignot, E., Binder, T., Blankenship, D., Drews, R., Eagles, G., et al. (2020) Deep glacial troughs and stabilizing ridges unveiled beneath the margins of the Antarctic ice sheet. *Nature Geoscience*, 13(2), 132–137. Available from: https://doi.org/10.1038/s41561-019-0510-8

Nishiizumi, K., Imamura, M., Caffee, M.W., Southon, J.R., Finkel, R.C. & McAninch, J. (2007) Absolute calibration of ^{10}Be AMS standards. *Nuclear Instruments and Methods in Physics Research Section B: Beam Interactions with Materials and Atoms*, 258(2), 403–413.

Norton, K.P., von Blanckenburg, F., Schlunegger, F., Schwab, M. & Kubik, P.W. (2008) Cosmogenic nuclide-based investigation of spatial erosion and hillslope channel coupling in the transient foreland of the Swiss Alps. *Geomorphology*, 95(3–4), 474–486. Available from: https://doi.org/10.1016/J.GEOMORPH.2007.07.013

Palmer, E.F., Licht, K.J., Swope, R.J. & Hemming, S.R. (2012) Nunatak moraines as a repository of what lies beneath the East Antarctic ice sheet. *Special Paper - Geological Society of America*, 487(March), 97–104. Available from: https://doi.org/10.1130/2012.2487(05)

Parrenin, F., Barnola, J.M., Beer, J., Blunier, T., Castellano, E., Chappellaz, J., et al. (2007) The EDC3 chronology for the EPICA Dome C ice core. *Climate of the Past*, 3(3), 485–497. Available from: https://doi.org/10.5194/cp-3-485-2007

Piccione, G., Blackburn, T., Tulaczyk, S., Rasbury, E.T., Hain, M.P., Ibarra, D.E., et al. (2022) Subglacial precipitates record Antarctic ice sheet response to late Pleistocene millennial climate cycles. *Nature Communications*, 13(1), 1–14. Available from: https://doi.org/10.1038/s41467-022-33009-1

Pollard, D. & Deconto, R.M. (2012) Description of a hybrid ice sheet-shelf model, and application to Antarctica. *Geoscientific Model Development*, 5(5), 1273–1295. Available from: https://doi.org/10.5194/gmd-5-1273-2012

Pritchard, H.D., Arthern, R.J., Vaughan, D.G. & Edwards, L.A. (2009) Extensive dynamic thinning on the margins of the Greenland and Antarctic ice sheets. *Nature*, 461(7266), 971–975. Available from: https://doi.org/10.1038/nature08471

Pritchard, H.D., Ligtenberg, S.R.M., Fricker, H.A., Vaughan, D.G., van den Broeke, M.R. & Padman, L. (2012) Antarctic ice-sheet loss driven by basal melting of ice shelves. *Nature*, 484(7395), 502–505. Available from: https://doi.org/10.1038/nature10968

Prothro, L.O., Majewski, W., Yokoyama, Y., Simkins, L.M., Anderson, J.B., Yamane, M., et al. (2020) Timing and pathways of East Antarctic Ice Sheet retreat. *Quaternary Science Reviews*, 230, 106166. Available from: https://doi.org/10.1016/J.QUASCIREV.2020.106166

Reese, R., Gudmundsson, G.H., Levermann, A. & Winkelmann, R. (2018) The far reach of ice-shelf thinning in Antarctica. *Nature Climate Change*, 8(1), 53–57. Available from: https://doi.org/10.1038/s41558-017-0020-x

Rignot, E., Mouginot, J. & Scheuchl, B. (2011) Ice flow of the Antarctic ice sheet. *Science (New York, N.Y.)*, 333(6048), 1427–1430. Available from: https://doi.org/10.1126/science.1208336

Schoof, C. (2007) Ice sheet grounding line dynamics: steady states, stability, and hysteresis. *Journal of Geophysical Research - Earth Surface*, 112(3), 1–19. Available from: https://doi.org/10.1029/2006JF000664

Seroussi, H., Nowicki, S., Payne, A.J., Goelzer, H., Lipscomb, W.H., Abe-Ouchi, A., et al. (2020) ISMIP6 Antarctica: a multi-model ensemble of the Antarctic ice sheet evolution over the 21st century. *The Cryosphere*, 14(9), 3033–3070. Available from: https://doi.org/10.5194/TC-14-3033-2020

Shipp, S., Anderson, J.B., Domack, E.W., Jacobson, E.A., Shipp, S. & Anderson, J.B. (1999) Late Pleistocene–Holocene retreat of the West Antarctic Ice-Sheet system in the Ross Sea: part 1—geophysical results. *GSA Bulletin*, 111(10), 1517–1536. Available from: https://doi.org/10.1130/0016-7606(1999)111<1486:LPHROT>2.3.CO;2

Small, D., Bentley, M.J., Jones, R.S., Pittard, M.L. & Whitehouse, P.L. (2019) Antarctic ice sheet palaeo-thinning rates from vertical transects of cosmogenic exposure ages. *Quaternary Science Reviews*, 206, 65–80. Available from: https://doi.org/10.1016/J.QUASCIREV.2018.12.024

Smith, B., Fricker, H.A., Gardner, A.S., Medley, B., Nilsson, J., Paolo, F.S., et al. (2020) Pervasive ice sheet mass loss reflects competing ocean and atmosphere processes. *Science*, 368(6496), 1239–1242. Available from: https://doi.org/10.1126/science.aaz5845

Spector, P., Stone, J., Cowdery, S.G., Hall, B., Conway, H. & Bromley, G. (2017) Rapid Early-Holocene deglaciation in the Ross Sea, Antarctica. *Geophysical Research Letters*, 44(15), 7817–7825. Available from: https://doi.org/10.1002/2017GL074216

Stearns, L.A., Smith, B.E. & Hamilton, G.S. (2008) Increased flow speed on a large East Antarctic outlet glacier caused by subglacial floods. *Nature Geoscience*, 1(12), 827–831. Available from: https://doi.org/10.1038/ngeo356

Stevens, C., Hulbe, C., Brewer, M., Stewart, C., Robinson, N., Ohneiser, C., et al. (2020) Ocean mixing and heat transport processes observed under the Ross Ice Shelf control its basal melting. *Proceedings of the National Academy of Sciences of the United States of America*, 117(29), 16799–16804. Available from: https://doi.org/10.1073/pnas.1910760117

Stewart, C.L., Christoffersen, P., Nicholls, K.W., Williams, M.J.M. & Dowdeswell, J.A. (2019) Basal melting of Ross Ice Shelf from solar heat absorption in an ice-front polynya. *Nature Geoscience*, 12(6), 435–440. Available from: https://doi.org/10.1038/s41561-019-0356-0

Stone, J.O., Balco, G.A., Sugden, D.E., Caffee, M.W., Sass, L.C., Cowdery, S.G., et al. (2003) Holocene deglaciation of Marie Byrd Land, West Antarctica. *Science (New York, N.Y.)*, 299(5603), 99–102. Available from: https://doi.org/10.1126/science.1077998

Stutz, J., Mackintosh, A., Norton, K., Whitmore, R., Baroni, C., Jamieson, S.S.R., et al. (2021) Mid-Holocene thinning of David Glacier, Antarctica: chronology and controls. *The Cryosphere*, 15(12), 5447–5471. Available from: https://doi.org/10.5194/TC-15-5447-2021

Sugden, D.E., Balco, G., Cowdery, S.G., Stone, J.O. & Sass, L.C. (2005) Selective glacial erosion and weathering zones in the coastal mountains of Marie Byrd Land, Antarctica. *Geomorphology*, 67(3–4), 317–334. Available from: https://doi.org/10.1016/J.GEOMORPH.2004.10.007

Todd, C., Stone, J., Conway, H., Hall, B. & Bromley, G. (2010) Late Quaternary evolution of Reedy Glacier, Antarctica. *Quaternary Science Reviews*, 29(11), 1328–1341. Available from: https://doi.org/10.1016/j.quascirev.2010.02.001

Venturelli, R.A., Siegfried, M.R., Roush, K.A., Li, W., Burnett, J., Zook, R., et al. (2020) Mid-Holocene grounding line retreat and Readvance at Whillans Ice Stream, West Antarctica. *Geophysical Research Letters*, 47(15), e2020GL088476. Available from: https://doi.org/10.1029/2020GL088476

Whitehouse, P.L., Bentley, M.J. & Le Brocq, A.M. (2012) A deglacial model for Antarctica: geological constraints and glaciological modelling as a basis for a new model of Antarctic glacial isostatic adjustment. *Quaternary Science Reviews*, 32, 1–24. Available from: https://doi.org/10.1016/j.quascirev.2011.11.016

Wilcken, K.M., Codilean, A.T., Fülöp, R.H., Kotevski, S., Rood, A.H., Rood, D.H., et al. (2022) Technical note: accelerator mass spectrometry of ^{10}Be and ^{26}Al at low nuclide concentrations. *Geochronology*, 4(1), 339–352. Available from: https://doi.org/10.5194/gchron-4-339-2022

Wilcken, K.M., Fujioka, T., Fink, D., Fülöp, R.H., Codilean, A.T., Simon, K., et al. (2019) SIRIUS performance: ^{10}Be, ^{26}Al and ^{36}Cl measurements at ANSTO. *Nuclear Instruments and Methods in Physics Research, Section B: Beam Interactions with Materials and Atoms*, 455, 300–304. Available from: https://doi.org/10.1016/j.nimb.2019.02.009

SUPPORTING INFORMATION

Additional supporting information can be found online in the Supporting Information section at the end of this article.

How to cite this article: Stutz, J., Eaves, S., Norton, K., Wilcken, K.M., Moore, C., McKay, R. et al. (2023) Inland thinning of Byrd Glacier, Antarctica, during Ross Ice Shelf formation. *Earth Surface Processes and Landforms*, 1–18. Available from: https://doi.org/10.1002/esp.5701